

CHARACTERISATION OF MARTIAN DUST AEROSOL PHASE FUNCTION FROM SKY RADIANCE MEASUREMENTS BY MSL ENGINEERING CAMERAS

H. Chen-Chen*, S. Pérez-Hoyos, A. Sánchez-Lavega

^aDepartamento de Física Aplicada I, Escuela de Ingeniería de Bilbao, Universidad del País Vasco (UPV/EHU). Bilbao 48013, Spain

* To whom correspondence should be addressed at: hao.chen@ehu.eus

Abstract

Dust is the main driver of Mars' atmospheric variability. The determination of Martian dust aerosol properties is of high relevance for radiative modelling and calculating its weather forcing. In particular, the light scattering behaviour at intermediate and large scattering angles can provide valuable information regarding the airborne dust particle shape. The angular distribution of sky brightness observed by the Mars Science Laboratory engineering cameras (Navcam and Hazcam) is used here to characterise the atmospheric dust single scattering phase function and to constrain the shape of the particles. An iterative radiative transfer based retrieval method was implemented in order to determine the aerosol modelling parameters which best reproduce the observed sky radiance as a function of the scattering angle in the solar almucantar plane. The aerosol models considered in this study for retrieving dust radiative properties were an analytical three term Double Henyey-Greenstein (DHG) phase function, T-matrix calculations for cylindrical particles with different diameter-to-length (D/L) aspect ratios and experimental phase functions from laboratory measurements of several Martian dust analogue samples. Results of this study returned mean DHG phase function parameter values $g_1 = 0.889 \pm 0.098$, $g_2 = 0.094 \pm 0.250$, $\alpha = 0.743 \pm 0.106$; generating a phase function with an asymmetry parameter of $g = 0.673 \pm 0.081$ (in line with Wolff et al., 2009). Although differences were observed during the low opacity aphelion season (lower forward scattering values, presence of a peak in the backward region) compared to the rest of the year, no clear evidences of seasonal behaviour or interannual variability were derived. The obtained average D/L aspect ratios for T-matrix calculated cylindrical particles were 0.70 ± 0.20 and 1.90 ± 0.20 (similar to Wolff et al., 2001), and the best fitting Martian dust analogue corresponded to the basalt sample (in agreement with Dabrowska et al., 2015).

1. Introduction

Dust is the main driver of the Martian atmospheric variability; it has a direct impact on the atmospheric thermal structure and provides forcing to its dynamics by absorbing and scattering solar radiation (Gierasch and Goody, 1972; Pollack et al., 1979). The importance of dust in Mars' climate has focused intensive research efforts on characterising its microphysical (e.g. particle size, shape, composition) and radiative (extinction efficiency, single scattering albedo, phase function) properties. Comprehensive reviews of results from previous studies can be found in Koralev et al. (2005), Smith et al. (2008). Because the radiative parameters depend on the microphysical properties of dust particles, the inversion of observation data to retrieve these parameters represents a challenging task (Pollack et al., 1995; Clancy et al., 2003; Wolff et al., 2009).

The single scattering phase function describes the angular distribution of the scattered light by aerosols and it is strongly influenced by the size and shape of the particles. In particular, the light scattering behaviour at intermediate and large scattering angles can provide relevant information on the aerosol particle shape (Kaufman et al., 1994). The characterisation of the particle shape is relevant as it affects the estimates of other parameters, such as the aerosol column optical thickness and the imaginary part of the refractive index (Dlugach et al., 2002). While light scattering calculations for spherical particles are straightforward by using the Lorenz-Mie theory (e.g. Hansen and Travis, 1974), calculations considering realistic dispersions of non-spherical particles may result very complex and computationally demanding (Dubovik et al., 2006; Yang et al., 2007; Yurkin and Hoekstra, 2007).

Retrievals of Martian atmospheric dust phase function and constraint of particle shape have been performed by several authors using both orbital observations and surface-based sky imaging data. Chýlek and Grams (1978) used a non-spherical randomly oriented particle model to fit Mariner 9 reflectance data during the 1971 Mars dust storm. Pollack et al. (1977, 1995) analysed Viking Lander sky images and used a semi-empirical theory to model scattering properties by non-spherical particles (Pollack and Cuzzi, 1980) for fitting the observations. They retrieved a modest peak in the backscattering region that suggested internal reflections by sharp corners within the particle's geometry associated to fluffy aggregates. Sky brightness data obtained by the Imager for Mars Pathfinder (IMP) were fitted with multiple scattering radiative transfer calculations to retrieve dust properties, including the single scattering phase function (Tomasko et al., 1999), and presented good agreements with plate-like particles (Markiewicz et al., 1999). Wolff et al. (2001) compared Mars Global Surveyor Thermal Emission Spectrometer (MGS TES) dust phase functions retrievals using radiative transfer simulations with T-matrix computations of non-spherical aerosols (Mishchenko et al., 1998) and obtained best-fits for randomly oriented cylinders with diameter-to-length (D/L) ratios of 2.3 or 0.6. Further comparisons using sky radiance data obtained by Mars Exploration Rover (MER) mission's Pancam instrument also derived similar results (Lemmon et al., 2004; Smith and Wolff, 2014).

All of these investigations have shown that light scattering by dust in Mars' atmosphere is consistent with non-spherical randomly oriented particles; however, the limited number of observations and the seasonal data coverage may only provide dust aerosol properties at the particular time and place of the observation. The objective of this work is to characterise Martian atmospheric dust scattering phase function using sky image data captured by the Mars Science Laboratory (MSL) engineering cameras and to contribute to previous studies by extending the results with observations for multiple seasons covering 4 Martian Years (MY 31 to 34).

The MSL mission have evaluated dust properties and its atmospheric loading at Gale Crater (4.6°S; 137.4°E) using different instrumentation (e.g., Lemmon et al. 2014; Smith et al., 2016; Vicente-Retortillo et al., 2017; McConnochie et al., 2017). Although not initially designed for scientific use, images retrieved by rover engineering cameras (navigation and hazard avoidance cameras) can be used as a complementary source of data for atmospheric studies (Soderblom et al. 2008; Smith and Wolff, 2014; Wolfe and Lemmon, 2015; Moores et al., 2015; Kloos et al., 2018). This study is a continuation of the work started in Chen-Chen et al. (2019), in which dust column optical depth and aerosol particle size were derived using MSL navigation cameras. In this case, the large field-of-view (FOV) offered by the hazard avoidance cameras, together with their capability to obtain simultaneous observations and their frequent use, make them suitable for studying dust light scattering properties at medium and large scattering angles.

This manuscript is structured as follows. In Section 2 the observation dataset is described and the processing details for the calibration and geometric reduction of MSL engineering camera images are provided. Section 3 describes the methodology used in this study, including the different aerosol models considered and the radiative transfer based retrieval procedure. In Section 4 the outcomes of this work are presented and discussed, together with the uncertainties and limitations of the method. Finally, in Section 5 a summary of the findings of this research and future prospects are given.

2. MSL engineering cameras observations

The MSL rover is equipped with a set of 12 engineering cameras: 4 navigation cameras (Navcam) and 8 hazard avoidance cameras (Hazcam). These cameras are build-to-print copies of MER engineering cameras and their objective is to provide guidance to the rover and support its operation during the drive across the surface. Navcams are located at the remote sensing mast and have a 45-degree FOV. The 8 Hazcams are fixed to the rover's chassis; they are located at the front (4) and rear (4) of the vehicle and have 124-degree square FOV optics (*fish-eye lens*). All imagers are equipped with a 1024x1024 pixel CCD detector and a broadband visible filter with an effective wavelength of 650 nm. For a complete description and technical specifications of these cameras we refer to Maki et al. (2012). The information related to the performance of the electronics and optics can be found in Maki et al. (2003).

2.1 Image sequences

Both MSL Hazcam and Navcam observation data were used in this study. In the case of Hazcam, we have taken advantage of their simultaneous front-rear pointing wide FOV imaging capability to retrieve the angular distribution of Martian sky brightness (**Figure 1, top**). For observations taken between local true solar time (LTST) 16:00 and 17:30, the corresponding solar elevation angle is approximately between 25° to 5° and the solar almucantar plane (circle of sky points with same elevation angle as the Sun) is contained within Hazcams' FOV. Depending on the rover's orientation and the surrounding topography, it is possible to retrieve the sky radiance as a function of the scattering angle with a 110° coverage and reaching up to 160° of scattering angle (maximum scattering angle in the solar almucantar plane is given by $\theta_{max} = 180^\circ - 2\epsilon_{Sun}$, where ϵ_{Sun} is the solar elevation angle). Therefore, the sampling of sky radiances along the solar almucantar direction was chosen for Hazcam observations. Part of the images had to be manually evaluated in order to discard unwanted contributions to the observed sky brightness curve (e.g., rover's chassis, robotic arm, rocks, and other scenery elements).

We have also considered for this study Navcam full sky-survey sequences (**Figure 1, bottom**). These datasets consist of multiple observations (usually 17 or 18 images) obtained in the early morning or afternoon in which the complete upper hemisphere was captured. The sky radiance as a function of the scattering angle was retrieved by sampling along the solar almucantar, in an analogous way as for Hazcam images. As the Navcam imagers are located at the rover's remote sensing mast, they have a more flexible pointing capability and the sky radiance curves were easily retrieved without the need of any further manual image analysis step. Only the possible intersections of the solar almucantar plane with *Aeolis Mons* (Mount Sharp) at the backscattering region, in the case of low Sun elevation observations, had to be taken into account when performing the data retrieval.

We show on **Figure 2**, for all the observation data retrieved along the solar almucantar, the contour plot of the sky radiance as a function of the scattering angle (θ) and the solar longitude (L_S). It can be appreciated that the sky brightness intensity and its angular distribution function follows a seasonal variation similar to the one derived for the dust column optical depth (e.g., Lemmon et al., 2014, Smith et al., 2016). The first part of the year (aphelion season) is characterised for its low dust activity and atmospheric optical depth; which can be also identified in the sky radiance curves, that show a steeper drop in the radiance values during this period ($L_S \sim 70^\circ$ to 140°) in the lateral scattering region ($\theta = 90^\circ$ to 120°), when compared to a flatter curve present during the high dust loading season, centred on $L_S = 200^\circ$.

The complete list of observations is provided on **Table A1** (on the Appendix).

2.2 Photometric calibration and geometric reduction

The raw EDR image files used in this work were converted from their original 12-bit pixel DN into physical units of absolute radiance ($\text{W m}^{-2} \text{ nm}^{-1} \text{ sr}^{-1}$). Once radiometrically calibrated, a geometric reduction was performed using the CAHVOR(E) photogrammetric camera model system (Yakimovsky and Cunningham, 1978; Gennery, 2006) in order to assign to each pixel their corresponding values of elevation and azimuth with respect to the local site reference frame (Peters, 2016). A detailed description of the radiometric calibration and geometric reduction of MSL Navcam observations can be found in Chen-Chen et al. (2019). An identical procedure was applied to MSL Hazcam images for this study and the specific calibration parameters for these cameras are provided in **Table 1**. The procedure derived for the calibration of MSL engineering cameras is based on the methodology developed by Soderblom et al. (2008) for the same instruments on-board the MER mission.

In order to validate Hazcam's calibration parameters, multiple comparisons of Navcam and Hazcam calibrated images were performed. Observation-pairs with similar pointing and near in LTST were selected for different sols and the absolute radiance values for same scenery features (e.g., sky, ground, Mount Sharp) were compared. The results of this procedure showed average differences of less than 5% between both imagers. As previous MSL Navcam absolute radiance uncertainty was estimated of about 12% (Chen-Chen et al., 2019), for this study we have considered Hazcam absolute radiance uncertainty of about 17%.

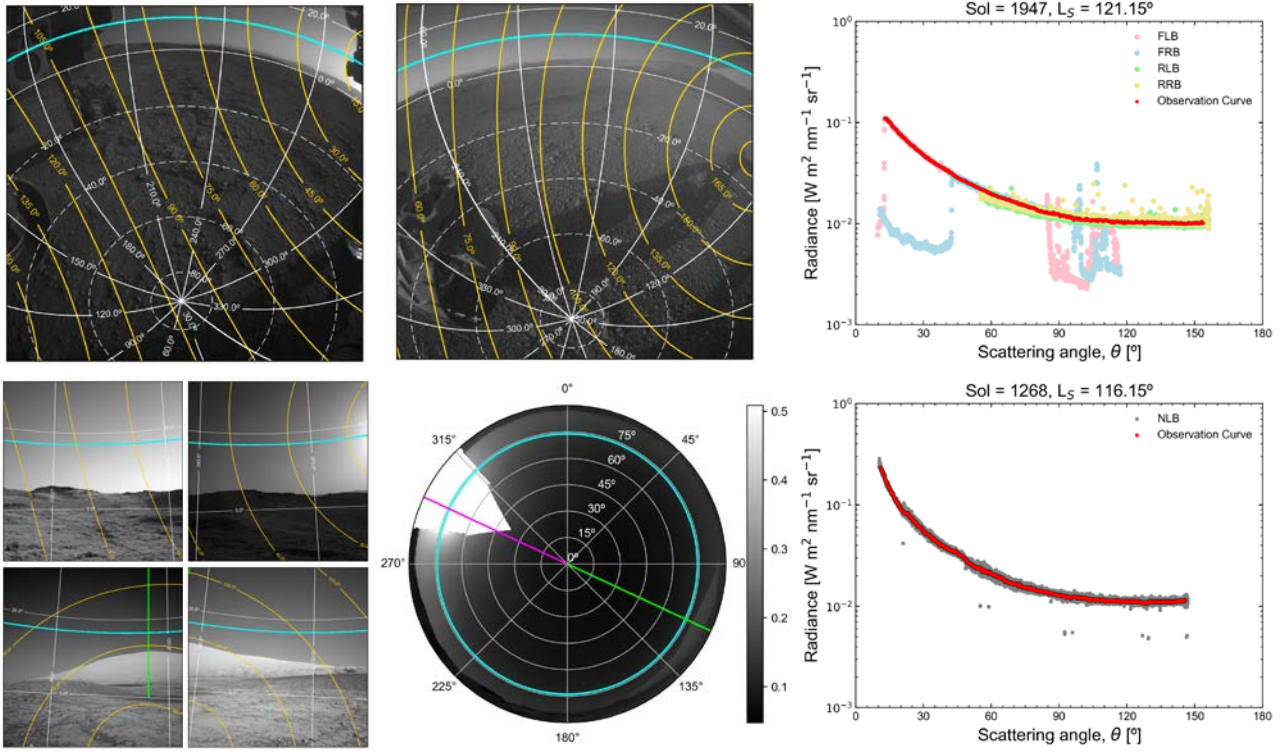


Figure 1. MSL engineering cameras observations. MSL Hazcam (top) and Navcam (bottom) images used for deriving the sky brightness angular distribution. The azimuth-elevation grid (white) with respect to a local site frame is shown, together with the scattering angles (yellow) and the solar almucantar plane (cyan). **Top:** Hazcam FLB (left) and RLB camera observations (centre) obtained on Sol 1947, $L_S=121.15^\circ$, LTST $\sim 17\text{h}$, with solar elevation angle of 11° . (Right) The sky radiance retrieved by all Hazcam cameras (FLB, FRB, RLB, RRB) along the solar almucantar plane and the final observation curve derived from these contributions. **Bottom:** (Left) Observations part of the Navcam sky-survey sequence retrieved on Sol 1268, $L_S=116.1^\circ$, LTST within 16:30 to 16:40, with Sun's elevation of 16° to 18° . (Centre) Polar-plot composition of the full sky-survey sequence, for clarity, the square root of radiance values is plotted. The almucantar (cyan) and solar principal plane's forward (magenta) and backward (green) region are also shown. On the right, the sky radiance sampled by each image of the Navcam sky-survey sequence on the solar almucantar (gray) and the final observation curve (red) are plotted. Additional data on the images are provided in Table A1 in the Appendix.

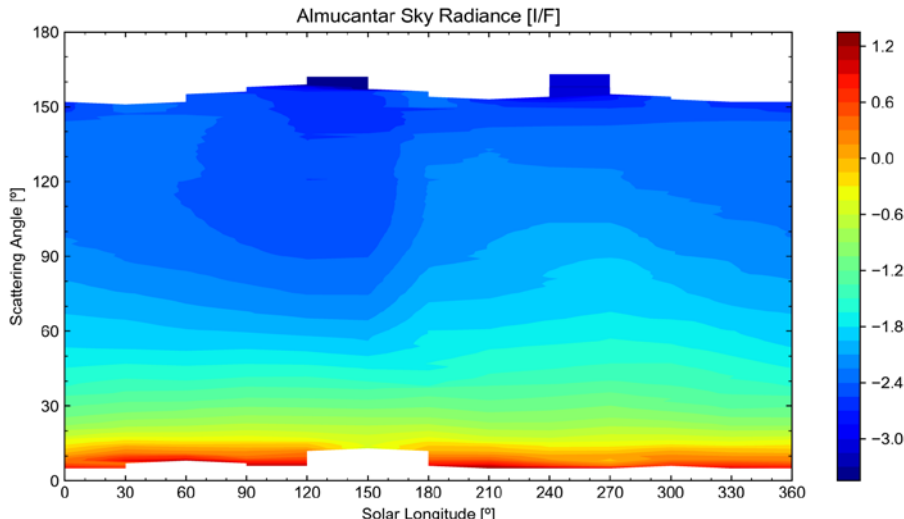


Figure 2. Seasonal variation of sky radiance as a function of the scattering angle. MSL engineering cameras retrieved sky brightness (expressed as radiance factor I/F , in logarithmic scale) in the solar almucantar plane, as a function of the scattering angle and the solar longitude. Radiance data binned every 1° of scattering angle and averaged over a 20° interval in L_S .

Table 1. MSL Hazard Avoidance Cameras (Hazcam) calibration parameters

CALIBRATION STAGE	MSL HAZARD AVOIDANCE CAMERAS CALIBRATION PARAMETERS ⁽⁰⁾				SOURCE
	FHAZ_LEFT_B: SN_0208	FHAZ_RIGHT_B: SN_0209	RHAZ_LEFT_B: SN_0212	RHAZ_RIGHT_B: SN_0207	
Bias removal	a0 = -25.45 DN, a1 = 36.5 DN, a2 = 0.0137 °C ⁻¹	a0 = -42.92 DN, a1 = 56.7 DN, a2 = 0.0104 °C ⁻¹ ,	a0 = -10.78 DN, a1 = 26.1 DN, a2 = 0.0302 °C ⁻¹ ,	a0 = -2.12 DN, a1 = 29.3 DN, a2 = 0.0277 °C ⁻¹ ,	Derived for MSL
Dark current removal: parameters	Masked region mean rate: c0 = 9.976 DN; c1 = 0.0992 °C ⁻¹ Active region mean rate: d0 = 17.877 DN, d1 = 0.0928 °C ⁻¹				Derived for MSL, PDS ⁽¹⁾
Masked dark flat image	FLB_388221706EDR_F, FLB_388221713EDR_F	FRB_388221706EDR_F, FRB_388221713EDR_F	RLB_388221950EDR_F, RLB_388221958EDR_F	RRB_388221950EDR_F, RRB_388221958EDR_F	PDS ⁽¹⁾⁽²⁾
Active dark flat image	FLB_388221720EDR_F, FLB_388221830EDR_F	FRB_388221720EDR_F, FRB_388221830EDR_F	RLB_388221965EDR_F, RLB_388221993EDR_F	RRB_388221965EDR_F, RRB_388221993EDR_F	PDS ⁽¹⁾⁽²⁾
Flat field correction	MSL_FLAT_SN_0208.IMG	MSL_FLAT_SN_0209.IMG	MSL_FLAT_SN_0212.IMG	MSL_FLAT_SN_0207.IMG	PDS ⁽³⁾
Conversion to physical units	K0 = 9.634e-6 W m ² nm ⁻¹ sr ⁻¹ (DN s ⁻¹) ⁻¹ ; K1 = 1.035e-8 W m ² nm ⁻¹ sr ⁻¹ (DN s ⁻¹) ⁻¹ °C ⁻¹				Adapted from MER ⁽⁴⁾

(0): Calibration parameters are defined in Chen-Chen et al. (2019) and references therein

(1): https://pds-imaging.jpl.nasa.gov/data/msl/MSLHAZ_0XXX/DATA/CRUISE/

(2): Dark masked and active flats are available in this public repository: <http://www.ajax.ehu.es/hcc/>

(3): https://pds-imaging.jpl.nasa.gov/data/msl/MSLHAZ_0XXX/CALIB/

(4): Table 2 from Soderblom et al., (2008). A 15% of uncertainty is assumed for K0 and K1 values.

3. Model and methodology

In this work the radiative transfer modelled sky brightness curves were iteratively compared to MSL Engineering Camera observations, in order to derive the parameters of the dust single scattering phase function generating the best fitting simulation. In the next paragraphs we describe the methodology followed to model the angular distribution of sky radiance and the comparison criterion used.

3.1 Radiative transfer model

The radiative transfer equation was solved using the discrete ordinates method (Stamnes et al., 1988) for a multiple scattering plane-parallel atmosphere. Simulations were performed using a Python version (PyDISORT, Ádámkovics et al., 2016) of DISORT 2.1 with pseudo-spherical correction (CDISORT, Buras et al., 2011). The atmosphere was modelled with 30 layers distributed in linearly spaced pressure levels with a total height of 100 km. Atmospheric parameter inputs (pressure, temperature, density, etc.) were retrieved from the Mars Climate Database (Forget et al., 1999; Millour et al., 2015). The main constituent species of Mars' atmosphere considered in our model (CO₂, H₂O, O₂, N₂ and O₃) present no strong gas absorption within the MSL cameras wavelength range (600 to 800 nm), so their contribution to the opacity was considered negligible. For the Rayleigh scattering due to the CO₂, the scattering cross section was obtained from the model and constants in Sneep and Ubachs (2005). These assumptions are the same as those taken in Chen-Chen et al. (2019).

3.2 Aerosol model

The radiative transfer computations required only 3 parameters at each layer of the discretised atmosphere model for the radiance: the aerosol single scattering albedo (ω_0), the single scattering phase function $P(\theta)$, and the vertical distribution of the aerosol optical depth, $\tau(z)$.

The dust optical depth at each layer $\tau(z)$ was modelled following a Conrath profile (Forget et al., 1999; Heavens et al., 2011), and the total column optical depth input value required in these profiles were retrieved from MSL Mastcam direct Sun imaging extinction measurements (Lemmon et al., 2014) and MSL Navcam retrievals (Chen-Chen et al., 2019).

For ω_0 and $P(\theta)$, we selected for this study the following 3 modelling approaches:

- *Analytical phase function.* A set of analytical single scattering phase functions were generated using a Double Henyey-Greenstein (DHG) three-parameter analytical expression (Kattawar et al., 1975; Gillespie, 1992) in the form of:

$$P_{DHG}(\theta) = \alpha \frac{1-g_1^2}{(1-2g_1\cos\theta+g_1^2)^{3/2}} + (1-\alpha) \frac{1-g_2^2}{(1-2g_2\cos\theta+g_2^2)^{3/2}} \quad (1)$$

Parameters controlling the forward scattering (g_1), backward scattering (g_2) and the forward-backward ratio (α) were varied in order to simulate different aerosol phase functions (Ignatov, 1997; Zhang and Li, 2016). The g_1 parameter was iterated from 0.50 to 1.00 with steps of 0.01; g_2 was varied between $-g_1$ and $+g_1$ (50 divisions) in order to prevent the backward scattering lobe from being greater than forward lobe and to avoid negative phase function values (Zhang and Li, 2016). Finally, the parameter controlling the ratio (α) was iterated from 0.50 to 1.00 (fully forward scattering case) with 0.01 steps. Again, this was set in order to control the overall shape of the phase function and use representatives of actual airborne dust phase functions (e.g., Mishchenko et al., 1997; Dubovik et al., 2006). The single scattering albedo was fixed to $\omega_0 = 0.975$ based on results derived from surface-orbit combined observations by Wolff et al. (2009) and particularised for MSL engineering cameras effective wavelength ($\lambda_{eff} \sim 650$ nm)

- *T-Matrix.* Previous studies have indicated the need to take into account the non-sphericity when modelling the optical properties of Martian dust (e.g., Pollack et al, 1977; Chylek and Grams, 1978). Although there are available multiple models for calculating the scattering properties of non-spherical particles, software codes for simulating particle shapes with complex and irregular geometry or large ensembles of particles are very computationally demanding (Yurkin and Hoekstra, 2007; Wriedt, 2009). We selected the T-matrix code (https://www.giss.nasa.gov/staff/mmishchenko/t_matrix.html) (Mishchenko et al., 1998) to calculate the radiative properties of randomly oriented cylindrical particles with different diameter-to-length (D/L) aspect ratios and sizes. The shape was fixed to cylindrical particles as the calculated phase functions for single aspect ratio cylinders do simulate well the usual airborne dust phase function in the lateral scattering region (θ approximately from 90° to 120°) (Mishchenko et al., 1997). This consideration avoided the need of introducing additional parameters associated to a distribution of aspect ratios when spheroidal particles are used, therefore reducing the number of comparisons to be performed and consequently the computation time of the retrieval. The aspect ratio parameter D/L was varied from 0.5 to 2.5, with steps of 0.1. The values of the single scattering albedo and phase function were calculated assuming a power law particle size distribution for volume equivalent effective radius (r_{eff}) varying from 0.10 to $1.70 \mu m$ in $0.02 \mu m$ steps (e.g., Chen-Chen et al., 2019), with effective variance $v_{eff} = 0.3$ (e.g. Mishchenko et al., 1997; Dubovik et al., 2006); the refractive complex index was derived from Wolff et al. (2009).

- *Laboratory measurements of Martian dust analogues.* Experimental measurements of single scattering phase functions for different Martian dust analogue samples were retrieved from the Amsterdam-Granada Light Scattering database (<https://www.iaa.csic.es/scattering/>) (Muñoz et al., 2012). The scattering phase functions at 647 nm for basalt, JSC0, JSC200, JSC-1A and palagonite samples were evaluated in this study. For a comprehensive description regarding the properties of the samples, experimental set up and retrieval of the scattering matrices we refer to the corresponding publications: basalt, JSC0 and JSC200 (Dabrowska et al., 2015); JSC-1A (Escobar-Cerezo et al., 2018) and palagonite (Laan et al., 2009). The single scattering albedo for each sample was approximated using the Lorenz-Mie theory (Mishchenko et al., 1995). For these computations, the particle size distribution parameters (r_{eff} , v_{eff}) and complex refractive index (m) of each sample were derived from the database: basalt ($r_{eff}=6.9 \mu m$, $v_{eff}=7.0$, $m=1.52+i0.001$), JSC0 ($r_{eff}=29.5 \mu m$, $v_{eff}=1.1$, $m=1.5+i0.001$), JSC200 ($r_{eff}=28.1 \mu m$, $v_{eff}=1.2$, $m=1.5+i0.001$), JSC-1A ($r_{eff}=15.85 \mu m$, $v_{eff}=2.28$, $m=1.65+i0.003$), palagonite ($r_{eff}=4.5 \mu m$, $v_{eff}=7.3$, $m=1.52+i0.0005$). The resulting single scattering albedos were: $\omega_{0,basalt}=0.892$, $\omega_{0,JSC0}=0.701$, $\omega_{0,JSC200}=0.633$, $\omega_{0,JSC1A}=0.708$ and $\omega_{0,palagonite}=0.960$.

We summarise on **Table 2** the dust aerosol models used in this work and their related parameters.

3.3 Retrieval procedure

An iterative retrieval scheme was implemented based on the comparison of radiative transfer simulations and MSL engineering camera observations of Martian sky brightness as a function of the scattering angle. A lowest mean quadratic deviation χ^2 criterion was considered for determining the best fitting curve.

For each Hazcam/Navcam observation:

1. Radiometric calibration and geometric reduction were performed as described in Section 2: for each image-pixel the corresponding values of absolute radiance, azimuth/elevation angles with respect to a Mars' local site reference system and the resulting scattering angle were calculated. The absolute radiance was then converted into approximated radiance factor (I/F) units by dividing each pixel's radiance value by the solar spectral irradiance at the top of the atmosphere at the time of the observation convolved to the Hazcam/Navcam bandpass (same for both imagers, $1.524 \text{ W m}^{-2} \text{ nm}^{-1} \text{ sr}^{-1}$ at 1 AU) and divided by π (e.g., Soderblom et al., 2008). The solar spectral irradiance data was obtained from Colina et al. (1996).

2. Retrieval of the observed sky brightness as a function of the scattering angle was performed by sampling radiance values along the solar almucantar plane.

3. The simulated sky brightness curves were generated using the radiative transfer model for different combinations of aerosol modelling parameters (**Table 2**) and allocated in a look-up-table (LUT).

5. The observed ($I/F_{obs}(\theta_i)$) sky radiance angular distribution function and the modelled ($I/F_{mod}(\theta_i)$) curves contained in the LUT were compared using a standard χ^2 least squares quadratic error criterion:

$$\chi^2 = \sum_{i=1}^N \left(\frac{I/F_{obs}(\theta_i) - I/F_{mod}(\theta_i)}{\sigma_i \cdot I/F_{obs}(\theta_i)} \right)^2 \quad (2)$$

For the N sampled points along the curve a variance of $\sigma_i = 0.20$ was used as a conservative value associated to the absolute calibration uncertainty for MSL engineering cameras considered in Section 2. The reduced χ^2 values (χ^2_{red}) were calculated by dividing the obtained χ^2 by the number of degrees of freedom $v = N - f$, where N is the number of sampled points and f the number of free parameters in the retrieval (f is equal to 3 for DHG, 2 for T-matrix and 1 for laboratory measurements) (**Table 2**)

6. The set of input parameters for each aerosol model generating the simulated sky brightness angular distribution with the minimum χ^2 value was considered the solution of the retrieval (**Figure 3**). The uncertainty level of the solution was estimated from the 68% confidence region (1σ error).

Table 2. Aerosol model parameters for radiative transfer simulations

Aerosol model	Single scat. albedo, ω_0	Phase function, $P(\theta)$		
		Parameters	Range	Reference
Double Henyey-Greenstein	0.975	Forward scattering (g_1), backward scattering (g_2), and ratio (α)	g_1 : 0.50 to 1.00, step of 0.01. g_2 : - g_1 to + g_1 , 50 divisions. α : 0.50 to 1.00, step of 0.01.	Zhang and Li, 2016
T-Matrix	Calculated	Cylindrical particles: diameter-to-length aspect ratio (D/L), size distribution effective radius (r_{eff})	D/L : 0.5 to 2.5, step of 0.1 r_{eff} : 0.10 to 1.70 μm , step of 0.02	Mishchenko et al., 1998.
Laboratory measurements	Calculated (Lorenz-Mie)	Martian dust analogue sample experimental phase functions at 647 nm.	Samples: Basalt, JSC0, JSC200, JSC-1A, Palagonite	Muñoz et al., 2012; Dabrowska et al. 2015; Escobar-Cerezo et al., 2018; Laan et al., 2009

4. Results and discussion

The methodology described in the previous Section was followed to retrieve the aerosol model parameters generating the best fitting sky radiance simulations. In this Section 4, the outcomes of the parameterisation scheme are presented. A discussion is provided for studying the seasonal behaviour and the interrelationships of the resulting parameters and the uncertainties of the retrieval are evaluated.

A summary table with the complete results of this study is provided on **Table A2** in the Appendix to this manuscript.

Double Henyey-Greenstein phase function parameters. The seasonal and interannual behaviour of the DHG analytical phase function parameters (g_1 , g_2 , α), and their interrelationships are shown on the left and right column on **Figure 5**, respectively. The average values retrieved for each parameter are: $g_1 = 0.889 \pm 0.098$, $g_2 = 0.094 \pm 0.250$ and $\alpha = 0.743 \pm 0.106$. When recurring to the expressions provided on Zhang and Li (2016), these parameter values generate a single scattering phase function with an asymmetry factor of $g = 0.687 \pm 0.081$, which is in good agreement with previous results by Wolff et al. (2009) at the 650 nm effective wavelength of MSL engineering cameras. It can be appreciated on **Figure 5** that results for Hazcam observations (red) show a greater dispersion and larger uncertainties than Navcam dataset outcomes (blue). This is mainly related to the pointing particularities of each set of cameras; while mast-mounted free pointing Navcam sky-surveys are capable of retrieving sky radiance curves covering scattering angles from approximately 10° to 150° , rover chassis fixed Hazcam observations are highly dependent on the geometry configuration at the specific LTST and location, thus retrieving image-sets with very different scattering angle coverage.

Regarding the seasonal variability of the DHG parameters, the results obtained during the low opacity aphelion season ($L_s \sim 40^\circ$ to 130°) show noticeable differences when compared to the rest of the year (the sensitivity to possible contribution from the aphelion cloud belt water-ice clouds in the retrieved sky radiance data during this particular season will be discussed below). In particular, the forward scattering parameter (g_1) values tend to be lower within this time. As phase function values in the forward scattering region ($\theta \sim 5^\circ$ to 30°) are related to the size of the particle (e.g., Kaufman, 1994; Tomasko et al., 1999), this may suggest the detection of smaller dust particles during this season. However, due to the differences in the scattering angle coverage by each observation, the lack of data in the forward scattering region may originate part of the dispersion in the results, therefore not providing strong evidences for identifying any particular seasonal behaviour. Seasonal differences can be also appreciated in the backward scattering parameter g_2 . In this case, the retrieved negative values are mostly located within the same aphelion period ($L_s \sim 40^\circ$ to 130°). DHG analytical phase functions with a $g_2 < 0$ are featured with a positive slope at the end of the backscattering region (minimum of phase function is at $\theta < 180^\circ$, existence of a peak). However, as in the previous case, the existing dispersion in the retrieved data does not allow to identify a clear seasonal behaviour for this parameter.

The interrelationships between the DHG parameters are shown at the right column of **Figure 5**. In this case, output charts tend to be more clear and results show a positive correlation for $g_1 - g_2$ parameters, and negative correlations for $g_1 - \alpha$ and $g_2 - \alpha$, being more evident in the latter case. The obtained negative correlations points out the role of the parameter α as weighting factor for controlling the overall shape of the DHG phase function; when large lobes in the function are obtained at the forward scattering area (g_1 close to 1) or at the backscattering (negative g_2), the parameter α tends to balance the counterpart region by shifting to 0.5 or 1.0, respectively.

Finally, regarding the interannual variability analysis, the different number of available observation data per MY and its seasonal distribution, sums up to the abovementioned dispersion of the retrieval results. Therefore it is not possible to conclude that any particular interannual behaviour was derived from the evaluated data.

Dust shape. The retrieval results for the diameter-to-length aspect ratio parameter for randomly oriented cylindrical particles calculated with T-matrix are shown on **Figure 6**. The frequency of aspect ratio counts returned average D/L values of 0.70 and 1.90 with an uncertainty of about 0.20, when differentiating D/L values larger and smaller than 1.0. These results present a good agreement with previous studies (e.g.: 0.60

or 2.30 by Wolff et al. (2001)). Regarding the seasonal evolution of this parameter, although average values tend to be slightly larger when only considering the low opacity aphelion season, it is not possible to conclude that the retrieved results show any seasonal variability.

Laboratory measurements of Martian dust analogues. The results of the observation-model comparison retrieval showed that only two models generated the best fitting model curve: basalt (78% of the cases) and palagonite (22%). This outcome is mainly related to the significant differences that exist in the particle size distribution of the available dust analogue samples ($r_{\text{eff,palagonite}} = 4.5 \mu\text{m}$, $r_{\text{eff,basalt}} = 6.9 \mu\text{m}$, , $r_{\text{eff,JSC1A}} = 15.85 \mu\text{m}$, $r_{\text{eff,JSC200}} = 28.1 \mu\text{m}$, $r_{\text{eff,JSC0}} = 29.5 \mu\text{m}$), where it can be appreciated that the effective radius parameter for the remaining analogues are about an order of magnitude larger than the usual values reported for Martian atmospheric dust aerosol (r_{eff} order of $\sim 1 \mu\text{m}$) by previous studies (Korablev et al., 2005; Smith, 2008; McConnochie et al., 2017; Chen-Chen et al., 2019). Previous studies comparing Martian airborne dust with experimental analogue measurements resulted in best fits to samples of palagonite (Clancy et al., 1995; Merikallio et al., 2013) and basalt (Dabrowska et al., 2015). No relevant seasonal or interannual variability in the best fitting basalt or palagonite dust samples were found.

The sensitivity of the retrieved DHG parameters to variations of the input values for the single scattering albedo, dust column optical depth and possible presence of water-ice clouds during the aphelion season was evaluated by performing several simulations for these scenarios (**Figure 4**).

Sensitivity to aerosol optical depth. The atmospheric column optical depth is a required input parameter for radiative transfer simulations. Regular measurements from MSL Mastcam afternoon direct Sun-imaging (Lemmon et al., 2014) and MSL Navcam near Sun-pointing observations (Chen-Chen, et al., 2019) were used. Dust column optical depth values were interpolated at the observation's sol (or L_s if there were no data available within a range of 20 sols), which could introduce some uncertainty in our retrieval procedure. The sensitivity of the results to uncertainties in column optical depth measurements was evaluated by simulating two scenarios containing 15% more and less dust atmospheric loading with respect to the nominal case. When the column optical depth was decreased, the analytical DHG phase function parameters g_1 , g_2 and α showed a difference of about 4%, 5% and 2.5% respectively with respect to the base scenario; whereas in the case of an increment of the dust extinction the resulting differences were of the order of 2%, 9% and 3%.

Sensitivity to single scattering albedo. The simulated sky brightness also depended on the input value of dust single scattering albedo (ω_0). As it has been abovementioned, for the case of analytical DHG phase functions the single scattering albedo was fixed to 0.975, which is a representative value for Martian dust (Wolff et al., 2009) at the effective wavelength of the cameras. The sensitivity of our retrieval procedure to variations in this parameter was evaluated by comparing the obtained results when the input ω_0 was set to of 0.940 (e.g., Tomasko et al., 1999). The resulting output parameters g_1 , g_2 and α varied in the order of 4%, 25% and 2%, respectively, with respect to the nominal scenario

Sensitivity to presence of water-ice clouds. Part of the observations used in this study were obtained during the aphelion season (centred on $L_s \sim 70^\circ$) and the possible presence of water-ice clouds from the aphelion cloud belt, developing around $L_s = 40^\circ - 60^\circ$ and dissipating near $L_s \sim 150^\circ$ (e.g., Clancy et al., 1996, 2003; Madeleine et al., 2012) might introduce deviations in the dust phase function parameters retrieval. Although the majority of the observations were taken before 7h or after 16h (LTST), when detections of water-ice clouds are very low and the reported optical depth is almost negligible (Kloos et al., 2018), the sensitivity of the results to this phenomenon was evaluated. For an observation retrieved on sol 1132 ($L_s = 54.2^\circ$) corresponding to MY 33 (high cloud detection at Gale Crater, e.g. McConnochie et al., 2017; Kloos et al., 2018), a simulation was performed in which a water-ice cloud was added to the base model: the optical depth of the cloud was set to $\tau_{\text{cloud}} = 0.15$ as a representative value of afternoon retrievals (Kloos et al., 2018), water-ice scattering properties Q_{ext} and ω_0 were derived from Warren (1984) and the single scattering phase function was modelled with an analytical DHG using water-ice representative parameters from Zhang and Li (2016). Differences between the simulated sky radiance as a function of the scattering angle for the base scenario and the water-ice cloud scenario were about 12% (lower than assumed uncertainty of 15%). When comparing with the observation for retrieving the parameters generating the best fitting curve, variations of the output g_1 , g_2 and α parameters of the DHG analytical phase function were of about 4.0%, 4.5% and 15.0%, respectively. The resulting simulated sky radiance curve including a water-ice cloud model and dust phase function are provided in **Figure 4**.

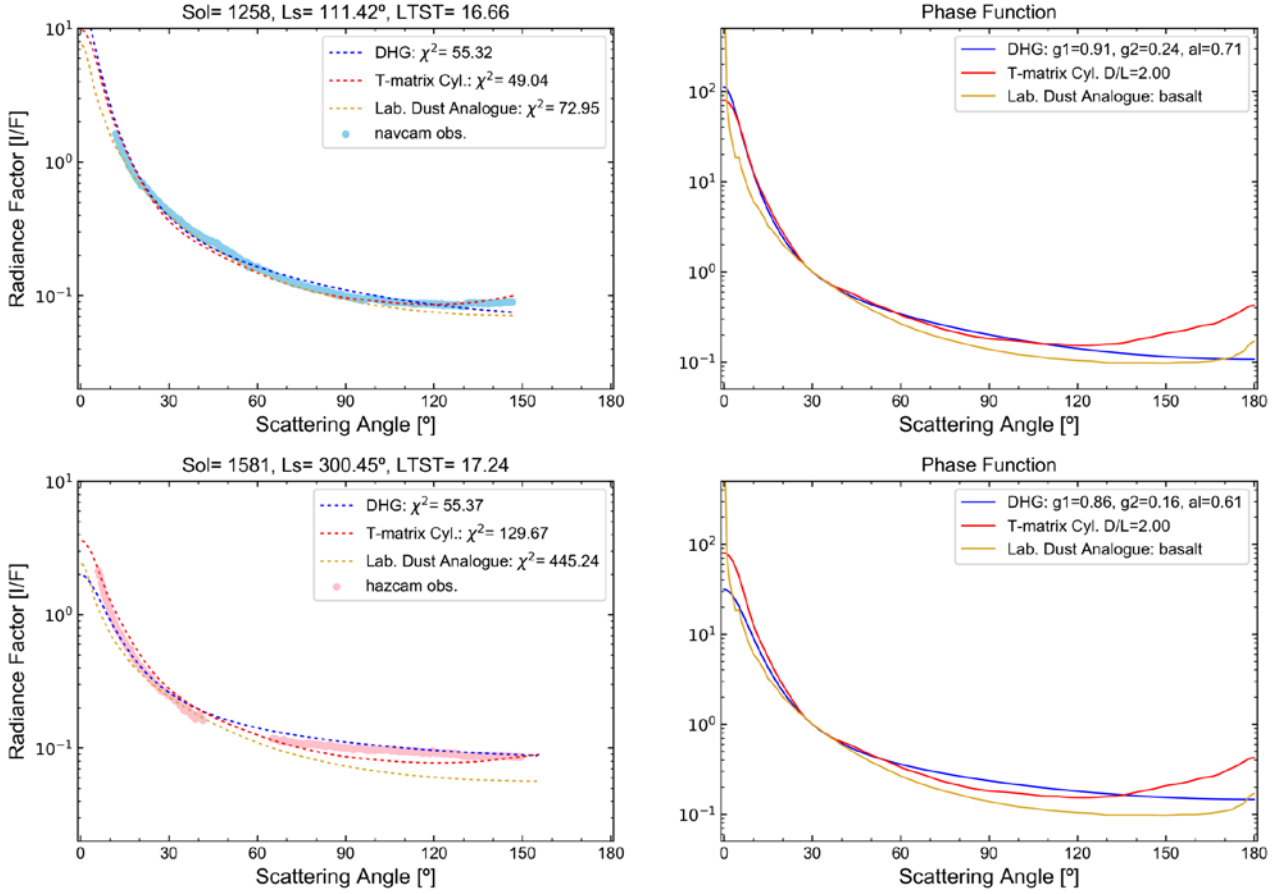


Figure 3. Comparison of observed and modelled sky brightness curves. Results of MSL Navcam (top) and Hazcam (bottom) observation comparisons to radiative transfer models: (left) the best fitting sky brightness as a function of the scattering angle simulations for the different aerosol models are provided; (right) the aerosol single scattering phase functions generating those best fitting curves. Phase functions are normalised to 1 at 30° scattering angle.

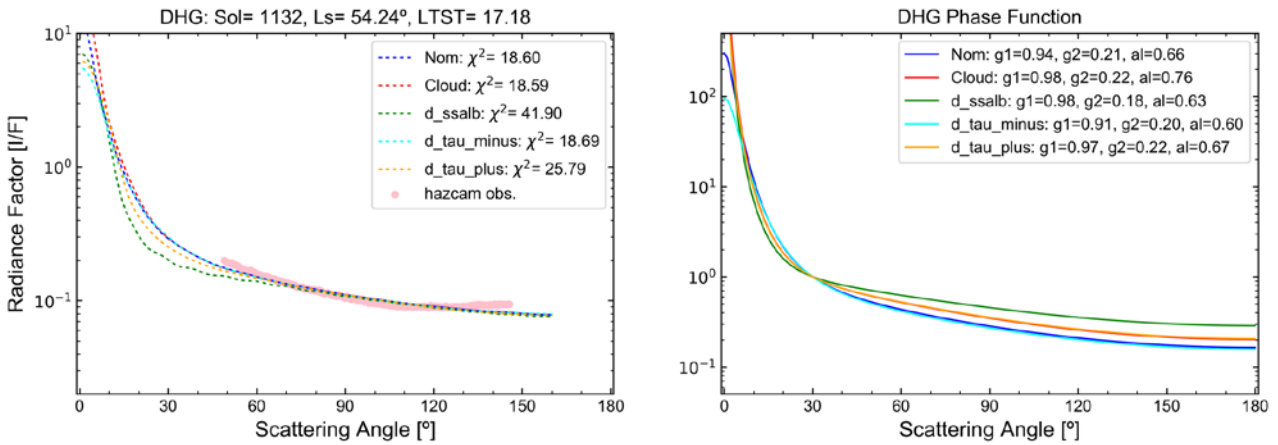


Figure 4. Sensitivity analysis of simulated sky brightness curves modelled with DHG aerosol phase functions. Outputs of DHG analytical phase function parameters (g_1 , g_2 , α) generating the best fitting sky brightness curve to MSL Hazcam observation corresponding to Sol 1132 ($L_s = 54.24^\circ$, MY 33), under different simulation cases: nominal scenario (blue), presence of water-ice cloud (red), single scattering albedo set to $\omega_0 = 0.94$ (green), nominal dust column optical depth input value decreased 25% (cyan) and increased 25% (yellow). On the right, modelled sky radiance angular distribution compared to observation; left, DHG single scattering phase function curves generation those simulations. Phase functions are normalised to 1 at 30° scattering angle.

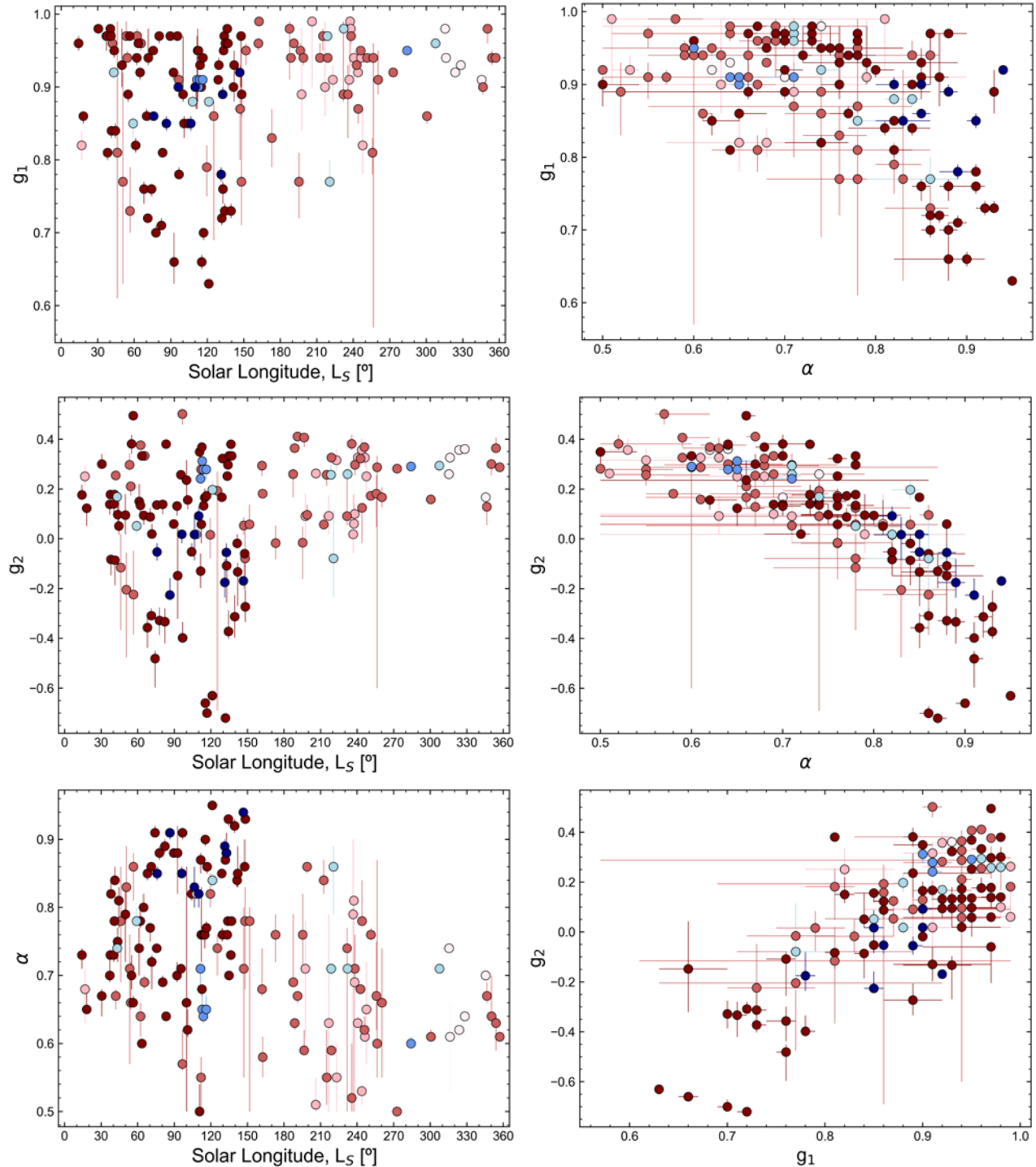


Figure 5. Double Henyey-Greenstein parameters seasonal variation and relationships. The seasonal behaviour (left column) and the existing interrelationships (right column) of the DHG analytical phase function parameters (g_1 , g_2 , α) generating the best fitting sky radiance model to MSL Navcam (blue) and Hazcam (red) observations. Colour shades indicate MY 31 (clearest) to MY 34 (darkest). No data for Navcam MY 31.

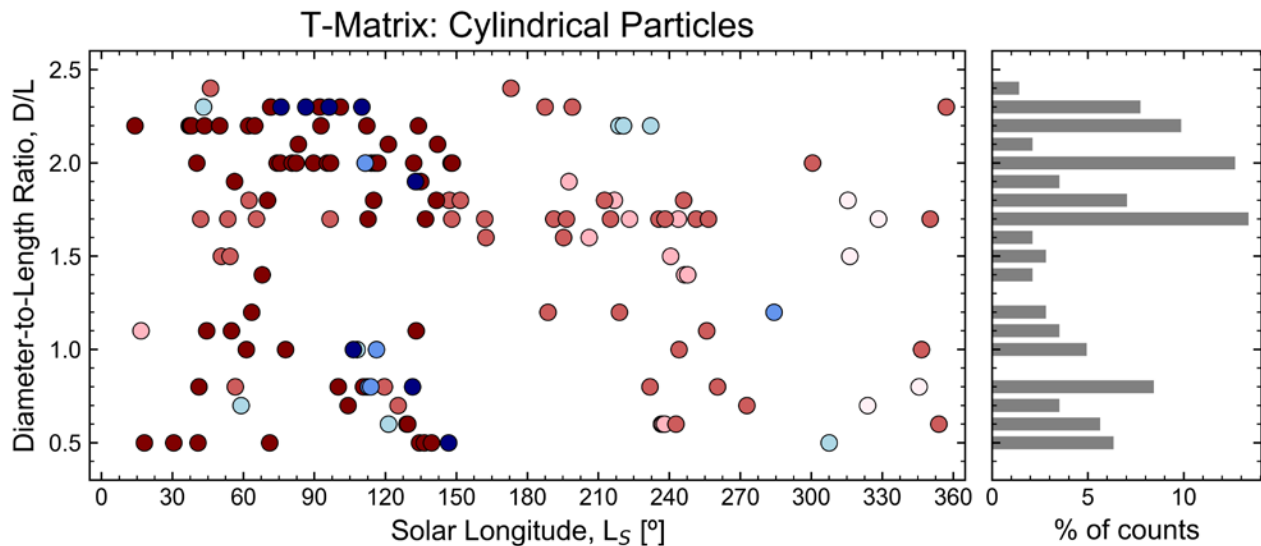


Figure 6. Seasonal and interannual variation of cylindrical particles aspect ratio. (Left) Results of T-matrix cylindrical particles diameter-to-length (D/L) aspect ratio parameter generating the best fitting sky radiance curve model to MSL Navcam (blue) and Hazcam (red) observations, as a function of the solar longitude and Martian Year (MY). Colour shades indicate MY 31 (clearest) to MY 34 (darkest). No data for Navcam MY 31. On the right, the bar chart shows the percentage of counts (frequency) for each D/L value.

5. Conclusion

In this study we have used sky radiance measurements in the almucantar plane obtained by the MSL Engineering Cameras to constrain the Martian dust single scattering phase function. Hazcam simultaneous forward-rear pointing opportunistic afternoon observations and Navcam sky-survey image sequences were selected and photometric calibration and geometric reduction were performed on the raw images. The angular distribution of sky radiance was retrieved for different seasons and Martian Years. These observations contained data for the intermediate and large scattering angle region, from 30° up to about 160°, where the light scattering due to the aerosol is dominated by the shape of the particle.

The observed sky brightness curves were iteratively compared with radiative transfer sky radiance simulations. The modelled sky radiance as a function of the scattering angle were calculated following a parameterisation scheme for defining the dust single scattering phase function using 3 different aerosol modelling approaches: a three term Double Henyey-Greenstein analytical function, T-matrix code calculations for cylindrical particles and using experimental laboratory retrievals of Martian dust analogues.

Results retrieved from the comparison procedure show average Double Henyey-Greenstein parameter values of $g_1 = 0.889 \pm 0.098$, $g_2 = 0.094 \pm 0.250$, $\alpha = 0.743 \pm 0.106$, which are related to a phase function with an asymmetry parameter of $g = 0.673 \pm 0.081$ (similar to, e.g., Wolff et al., 2009). Existing seasonal differences for the low dust opacity aphelion season (L_s 30° to 150°) were observed for g_1 and g_2 , although it was not possible to derive a clear seasonal or interannual behaviour, due mainly to the dispersion in the results and the different seasonal distribution of the data. Best fitting diameter-to-length aspect ratios for T-matrix cylindrical particles were of 0.70 ± 0.20 and 1.90 ± 0.20 , presenting a good agreement with previous studies (Wolff et al., 2001). Comparisons with experimental single scattering phase functions of dust analogues returned only two different best fitting samples, basalt (78%) and palagonite (22%), in line with Dabrowska et al., 2015.

Future research prospects include the retrieval and processing of observations under heavy dust loading scenarios, such as the global dust storm event in 2018, in order to evaluate the influence of such conditions in the dust single scattering phase function when compared to regular MY. On the aerosol modelling side, further developments can be done in the computation codes and methods for simulating the aerosol radiative properties for more realistic dust particles with complex shapes (e.g.; Yurkin and Hoekstra, 2007; Meng et al., 2007; Pitman et al., 2000). In addition to this, further comparisons can be performed for a broader variety of laboratory retrievals of Martian dust analogue single scattering measurements, with adequate particle size distributions, closer to the values retrieved for the atmospheric dust.

Acknowledgements

This work was supported by the Spanish project AYA2015-65041-P with FEDEER support, Grupos Gobierno Vasco IT-765-13, and Diputación Foral de Bizkaia - Aula EspaZio Gela. We wish to thank Professor Mark T. Lemmon for providing the MSL Mastcam optical depth values.

References

- Ádámkovics, M., Mitchell, J. L., Hayes, A. G., Rojo, P. M., Corlies, P., Barnes, J. W., Ivanov, V. D., Brown, R. H., Baines, K. H., Burrati, B. J., Clark, R. N., Nicholson, P. D., and Sotin, C. Meridional variation in tropospheric methane on Titan observed with AO spectroscopy at Keck and VLT, *Icarus*, 270, 376-388, doi: 10.1016/j.icarus.2015.05.023 (2016)
- Buras, R., Dowling, T., and Emde, C. New secondary-scattering correction in DISORT with increased efficiency for forward scattering, *Journal of Quantitative Spectroscopy and Radiative Transfer*, Volume 112, Issue 12, 2028-2034, doi: 10.1016/j.jqsrt.2011.03.019 (2011)
- Chen-Chen, H., Pérez-Hoyos, S., and Sánchez-Lavega, A. Dust particle size and optical depth on Mars retrieved by the MSL Navigation Cameras, *Icarus*, 319, 43-57, doi: 10.1016/j.icarus.2018.09.010 (2019)
- Chýlek, P., and Grams, G. W. Scattering by Nonspherical Particles and Optical Properties of Martian Dust, *Icarus*, volume 36, issue 2, 198-203, doi: 10.1016/0019-1035(78)90104-5 (1978)
- Clancy, R. T., Lee, S. W., Gladstone, G. R., McMillan, W. W., and Rousch, T. A new model for Mars atmospheric dust based upon analysis of ultraviolet through infrared observations from Mariner 9, Viking, and Phobos, *J. Geophys. Res.*, 100, 5251-5264, doi: 10.1029/94JE01885 (1995)
- Clancy, R. T., Grossman, A. W., Wolff, M. J., James, P. B., Rudy, D. J., Billawala, Y. N., Sandor, B. J., Lee, S. W., and Muhleman, D. O. Water vapour saturation at low altitudes around Mars aphelion: a key to Mars climate?, *Icarus*, 122, 36-62, doi: 10.1006/icar.1996.0108 (1996)
- Clancy, R. T., Wolff, M. J., and Christensen, P. R. Mars aerosol studies with the MGS TES emission phase function observations: Optical depths, particle sizes, and ice cloud types versus latitude and solar longitude, *J. Geophys. Res.*, vol. 108, E9, 5098, doi: 10.1029/2003JE002058 (2003)
- Colina, L., Bohlin, R. C., and Castelli, F. The 0.12-2.5 micron absolute flux distribution of the Sun for comparison with solar analogue stars, *Astron. J.*, 112, 307-314, doi: 10.1086/118016 (1996)
- Dabrowska, D. D., Muñoz, O., Moreno, F., Ramos, J. L., Martínez-Frías, J., and Wurm, G. Scattering matrices of martian dust analogs at 488 nm and 647 nm, *Icarus*, 250, 83-94, doi: 10.1016/j.icarus.2014.11.024 (2015)
- Dlugach, Z. M., Mishchenko, M. I., and Morozhenko, A. V. The effect of the shape of dust aerosol particles in the Martian atmosphere on the particle parameters, *Solar Sys. Res.*, 36, 367-373, doi: 10.1023/A:1020459320523 (2002)
- Dubovik, O., Sinyuk, A., Lapyonok, T., Holben, B. N., Mishchenko, M., Yang, P. Eck, T. F., Volten, H., Muñoz, O., Veihelmann, B., van der Zande, W. J., Leon, J.-F., Sorokin, M., and Slutsker, I. Application of spheroid models to account for aerosol particle nonsphericity in remote sensing of desert dust, *J. Geophys. Res.*, 111, D11208, doi:10.1029/2005JD006619 (2006)
- Escobar-Cerezo, J., Muñoz, O., Moreno, F., Guirado, D., Gómez Martín, J. C., Goguen, J. D., Garboczi, E. J., Chiaramonti, A. N., Lafarge, T., and West, R. A. An Experimental Scattering Matrix for Lunar Regolith Simulant JSC-1A at Visible Wavelengths, *The Astrophysical Journal Supplement Series*, 235, 19-27, doi: 10.3847/1538-4365 (2018)
- Forget, F., Hourdin, F., Fournier, R., Hourdin, C., Talagrand, O., Collins, M., Lewis, S. R., Read, P. L., and Huot, J.-P. Improved general circulation models of the Martian atmosphere from the surface to above 80 km, *J. Geophys. Res.*, 104, 24155–24175 (1999)
- Gennery, D. B. Generalized camera calibration including fish-eye lenses, *Int. J. Comput. Vis.*, 68(3), 239-266, doi: 10.1007/s11263-006-5168-1 (2006)

Gierasch, P. G., and Goody, R. M. The effect of dust on the temperature of the Martian atmosphere, *J. Atmos. Sci.*, 29, 400-402 (1972)

Gillespie, P. An analytic phase function for cylindrical particles, U.S. Army Atmospheric Sciences Laboratory, ASL-TR-0318, U.S. Army Laboratory Command (1992)

Hansen, J. E., and Travis, L. D. Light scattering in planetary atmospheres, *Space Sci. Rev.*, 16, 527-610 (1974)

Heavens, N. G., Richardson, M. I., Kleinböhl, A., Kass, D. M., McCleese, D. J., Abdou, W., Benson, J. L., Schofield, J. T., Shirley, J. H., and Wolkenberg, P. M. The vertical distribution of dust in the Martian atmosphere during northern spring and summer: Observations by the Mars Climate Sounder and analysis of zonal average vertical dust profiles, *J. Geophys. Res.*, 116, E04003, doi: 10.1029/2010JE003691 (2011)

Ignatov, A. Estimation of the aerosol phase function in backscatter from simultaneous satellite and Sun-photometer measurements, *Journal of applied meteorology*, 36, 688-694, doi: 10.1175/1520-0450(1997)036<0688:EOTAPF>2.0.CO;2 (1997)

Kaufman, Y. J., Gitelson, A. J., Karniel, A., Ganor, E., Fraser, R. S., Nakajima, T., Mattoo, S., and Holben, B. N. Size distribution and scattering phase function of aerosol particles retrieved from sky brightness measurements, *J. Geophys. Res.*, 99 (D5), 10341-10356, doi: 10.1029/94JD00229 (1994)

Kattawar, G. W. A three-parameter analytic phase function for multiple scattering calculations. *Journal of Quantitative Spectroscopy and Radiative Transfer*, Volumen 15, Issue 9, 839-849, doi: 10.1016/0022-4073(75)90095-3 (1975)

Kloos, J. L., Moores, J. E., Whiteway, J. A., and Aggarwal, M. Interannual and diurnal variability in water ice clouds observed from MSL over two Martian Years, *Journal of Geophysical Research: Planets*, 123, 233-245, doi: 10.1002/2017JE005314 (2018)

Korablev, O., Moroz, V. I., Petrova, E. V., and Rodin, A. V. Optical properties of dust and the opacity of the Martian atmosphere, *Adv. Space. Res.*, 35, 21-30, doi: 10.1016/j.asr.2003.04.061 (2005)

Laan, E. C., Volten, H., Stam, D. M., Muñoz, O., Hovenier, J. W., and Roush, T. L. Scattering matrices and expansion coefficients of martian analogue palagonite particles, *Icarus*, 199, 219-230, doi: 10.1016/j.icarus.2008.08.011 (2009)

Lemmon, M. T., Wolff, M. J., Smith, M. D., Clancy, R. T., Banfield, D., Landis, G. A., Ghosh, A., Smith, P. H., Spanovich, N., Whitney, B., Whelley, P., Greeley, R., Thompson, S., Bell III, J. F., and Squyres, S. W. Atmospheric imaging results from the Mars Exploration Rovers: Spirit and Opportunity, *Science*, 306, 1753-1756, doi: 10.1126/science.1104474 (2004)

Lemmon, M. T. The Mars Science Laboratory optical depth record. Eighth International Conference on Mars. Abstract #1338. 2014LPICo1791.1338L (2014)

Madeleine, J.-B., Forget, F., Spiga, A., Wolff, M. J., Montmessin, F., Vincendon, M., Jouglet, D., Gondet, B., Bibring, J.-P., Langevin, Y., and Schmitt, B. Aphelion water-ice cloud mapping and property retrieval using the OMEGA imaging spectrometer onboard Mars Express, *J. Geophys. Res. Planets*, 117 (E11), pp. E00J07, doi: 10.1029/2011JE003940 (2012)

Maki, J. N., Bell III, J. F., Herkenhoff, K. E., Squyres, S. W., Kiely, A., Klimesh, M., Schwuchert, M., Litwin, T., Willson, R., Johnson, A., Maimone, M., Baumgartner, E., Collins, A., Wadsworth, M., Elliot, S. T., Dingizian, A., Brown, D., Hagerott, E. C., Scherr, L., Deen, R., Alexander, D., and Lorre, J. Mars Exploration Rover Engineering Cameras, *J. Geophys. Res.*, 108, 8071, doi: 10.1029/2003JE002077 (2003)

Maki, J. N., Thiessen, D., Pourangi, A., Kobzeff, P., Litwin, T., Scherr, L., Elliot, S., Dingizian, A., and Maimone, M. The Mars Science Laboratory Engineering Cameras, Space Sci. Rev., 170, 77-93, doi:10.1007/s11214-012-9882-4 (2012)

Markiewicz, W. J., Sablotny, R. M., Keller, H. U., Thomas, N., Titov, D., Smith, P. H. Optical properties of the Martian aerosols as derived from Imager for Mars Pathfinder midday sky brightness data, J. Geophys. Res., 104(E4), 9009–9017, doi:10.1029/1998JE900033 (1999)

McConnochie, T. H., Smith, M. D., Wolff, M. J., Bender, S., Lemmon, M., Wiens, R. G., Maurice, S., Gasnault, O., Lasue, J., Meslin, P.-Y., Harri, A.-M., Genzer, M., Kemppinen, O., Martínez, G. M., DeFlores, L., Blaney, D., Johnson, J. R., and Bell III, J. F. Retrieval of water vapour column abundance and aerosol properties from ChemCam passive sky spectroscopy, Icarus 2017, doi: 10.1016/j.icarus.2017.10.043 (2017)

Meng, Z., Yang, P., Kattawar, G. W., and Bi, L. Single-scattering properties of tri-axial ellipsoidal mineral dust aerosols: A database for application to radiative transfer calculations, Journal of Aerosol Science 41(5), pp. 501-512, doi: 10.1016/j.jaerosci.2010.02.008 (2010)

Merikallio, S., Nousiainen, T., Kahnert, M., and Harri, A.-M. Light scattering by the Martian dust analog, palagonite, modeled with ellipsoids, Opt. Express, 21, 17972-17985, doi: 10.1364/OE.21.017972 (2013)

Millour, E., Forget, F., Spiga, A., Navarro, T., Madeleine, J. B., Montabone, L., Pottier, A., Lefevre, F., Montmessin, F., Chaufray, J. Y., Lopez-Valverde, M. A., Gonzalez-Galindo, F., Lewis, S. R., Read, P. L., Huout, J.-P., Desjean, M. C., and the MCD/GCM development team. The Mars Climate Database (MCD version 5.2), EPSC Abstracts, Vol. 10, EPSC2015-438 (2015)

Mishchenko, M. I., Lacis, A. A., Carlson, B. E., and Travis, L. D. Nonsphericity of dust-like tropospheric aerosols: implications for aerosol remote sensing and climate modelling, Geophys. Res. Lett., 22 (9), 1077-1080, doi: 10.1029/95GL00798 (1995)

Mishchenko, M. I., L. D. Travis, R. A. Kahn, and R. A. West, Modeling phase functions for dustlike tropospheric aerosols using a shape mixture of randomly oriented polydisperse spheroids, J. Geophys. Res., 102(D14), 16,831 – 16,848. (1997)

Mishchenko, M. I., and Travis, L. D. Capabilities and limitations of a current Fortran implementation of the T-Matrix method for randomly oriented, rotationally symmetric scatterers, J. Quant. Spectrosc. Radiat. Transfer, Vol. 60, No. 3, pp. 309-324, doi: 10.1016/S0022-4073(98)00008-9 (1998).

Moores, J. E., Lemmon, M. T., Kahanpää, H., Rafkin, S. C. R., Francis, R., Pla-García, J., Bean, K., Haberle, R., Newman, C., Mischna, M., Vasavada, A. R., de la Torre-Juárez, M., Renno, N., Bell, J., Calef, F., Cantor, B., McConnochie, T. H., Harri, A.-M., Genzer, M., Wong, M. H., Smith, M. D., Martín-Torres, F. J., Zorzano, M.-P., Kemppinen, O., and McCullough, E. Observational evidence of a suppressed planetary boundary layer in northern Gale Crater, Mars as seen by the Navcam instrument onboard the Mars Science Laboratory rover, Icarus, 249, 129 – 142, doi: 10.1016/j.icarus.2014.09.020 (2015)

Muñoz, O., Moreno, F., Guirado, D., Dabrowska, D. D., Volten, H., and Hovenier, J. W. The Amsterdam-Granada Light Scattering Database, Journal of Quantitative Spectroscopy and Radiative Transfer, Vol. 113, Issue 7, pp. 565-574, doi: 10.1016/j.jqsrt.2012.01.014 (2012)

Peters, S. Mars Science Laboratory Pointing, Positioning, Phasing, and Coordinate Systems (PPPCS) Document, Volume 9, Surface Remote Sensing and Navigation (2016)

Pitman, K. M., Wolff, M. J., Clancy, R. T., and Clayton, G. C. On the shape of martian dust and water ice aerosols, Abstract AAS-DPS Meeting 32, id. 51.09, Bulletin of the American Astronomical Society, Vol. 32, p. 1095 (2000)

Pollack, J. B., Colburn, D., Kahn, R., Hunter, J., Van Camp, W., Carlston, C. E., and Wolf, M. R. Properties of aerosols in the Martian atmosphere, as inferred from Viking Lander imaging data, *J. Geophys. Res.*, Volume 82, Issue 28, doi: 10.1029/JS082i028p04479 (1977)

Pollack, J. B., Colburn, D. S., Flasar, F. M., Kahn, R., Carlston, C. E., and Pidek, D. G. Properties and effects of dust particles suspended in the Martian atmosphere, *J. Geophys. Res.*, 84, 2929-2945 (1979)

Pollack, J. B., and Cuzzi, J. N. Scattering by nonspherical particles of size comparable to a wavelength: a new semi-empirical theory and its application to tropospheric aerosols, *J. Atmos. Sci.*, 37, 868-881, doi: 10.1175/1520-0469(1980)037<0868:SBNPOS>2.0.CO;2 (1980)

Pollack, J. B., Ockert-Bell, M. E., and Shepard, M. K. Viking Lander image analysis of Martian atmospheric dust, *J. Geophys. Res.*, 100, E3, 5235-5250, doi: 10.1029/94JE026-40 (1995)

Smith, M. D. Spacecraft observations of the Martian atmosphere, *Annu. Rev. Earth Planet. Sci.* 36, 191-219, doi: 10.1146/annurev.earth.36.031207.124334 (2008)

Smith, M. D., Zorzano, M.-P., Lemmon, M., Martín-Torres, J., and Mendaza de Cal, T. Aerosol optical depth as observed by the Mars Science Laboratory REMS UV photodiodes, *Icarus*, vol. 280, 234-248 (2016)

Smith, M. D., and Wolff, M. J. Dust aerosol particle size and shape using MER NAVCAM and PANCAM sky imaging, The 5th International Workshop on the Mars Atmosphere: Modelling and Observation (MAMO 5th), Abstract #2101. 2014mamo.conf.2101S (2014)

Sneep, M., and Ubachs, W. Direct measurements of the Rayleigh scattering cross section in various gases, *Journal of Quantitative Spectroscopy and Radiative Transfer*, Volume 92, Issue 3, p. 293-310, doi: 10.1016/j.jqsrt.2004.07.025 (2005)

Soderblom, J. M., Bell III, J. F., Johnson, J. R., Joseph, J. and Wolff, M. J. Mars Exploration Rover Navigation Camera in-flight calibration, *J. Geophys. Res.*, 113, E06S19, doi: 10.1029/2007JE003003 (2008)

Stamnes, K., Tsay, S.-C., Wiscombe, W., and Jayaweera, K. Numerically stable algorithm for discrete-ordinate-method radiative transfer in multiple scattering and emitting layered media, *Appl. Opt.* 27, 2502-2509 (1988)

Tomasko, M. G., Doose, L. R., Lemmon, M., Smith, P. H., and Wegryn, E. Properties of dust in the Martian atmosphere from the Imager on Mars Pathfinder, *J. Geophys. Res.*, 104, 8987-9007, doi: 10.1029/1998JE900016 (1999)

Vicente-Retortillo, A., Martínez, G. M., Renno, N. O., Lemmon, M. T., and de la Torre-Juárez, M. Determination of dust aerosol particle size at Gale Crater using REMS UVS and Mastcam measurements, *Geophys. Res. Lett.*, 44, 3502-3508, doi: 10.1002/2017GL072589 (2017)

Warren, S. G. Optical constants of ice from the ultraviolet to the microwave, *Applied Optics*, Vol. 23, Issue 8, pp. 1206 – 1225, doi: 10.1364/AO.23.001206 (1984)

Wolfe, C. A., and Lemmon, M. T. Using Engineering Cameras on Mars landers and rovers to retrieve atmospheric dust loading, 46th Lunar and Planetary Science Conference, Abstract #2851 (2015)

Wolff, M. J., Clancy, R. T., Pitman, K. M., Bell, J. F., and James, P. B. Constraints on Martian Aerosol Particles Using MGS/TES and HST Data: Shapes, American Geophysical Union (AGU), Fall Meeting 2001, abstract id.P32E-05 (2001)

Wolff, M. J., Smith, M. D., Clancy, R. T., Arvidson, R., Kahre, M., Seelos IV, F., Murchie, S., and Savijärvi, H. Wavelength dependence of dust aerosol single scattering albedo as observed by the compact reconnaissance imaging spectrometer, *J. Geophys. Res.*, 114, E00D04, doi:10.1029/2009JE003350 (2009)

Wriedt, T. Light scattering theories and computer codes, *J. Quant. Spectrosc. Radiat. Trans.*, 110, 833-843, doi: 10.1016/j.jqsrt.2009.02.023 (2009)

Yakimovsky, Y., and Cunningham, R. A system for extracting three-dimensional measurements from a stereo pair of TV cameras, *Computer Graphics and Image Processing*, 7, 195-210, doi: 10.1016/0146-664X(78)90112-0

Yang, P., Fent, Q., Hong, G., Kattawar, G. W., Wiscombe, W. J., Mishchenko, M. I., Dubovik, O., Laszlo, I., and Sokolik, I. N. Modeling of the scattering and radiative properties of nonspherical dust-like aerosols, *Journal of Aerosol Science*, Volume 41, Issue 11, pp. 1052-1053, doi: 10.1016/j.aerosci.2007.07.001 (2007)

Yurkin, M. A., and Hoekstra, A. G. The discrete dipole approximation: an overview and recent developments, *J. Quant. Spectrosc. Radiat. Transf.* 106, 558-589, doi: 10.1016/j.jqsrt.2007.01.034 (2007)

Zhang, F., and Li, J. A note on double Henyey-Greenstein phase function, *Journal of Quantitative Spectroscopy and Radiative Transfer*, Volume 184, p. 40-43, doi: 10.1016/j.jqsrt.2016.06.016 (2016)

APPENDIX A

Table A1. MSL Engineering Camera observations

Sol	Ls[°]	MY	LTST	Sun Azim. [°]	Sun Elev. [°]	Camera	SCLK/Sequence
269	315.37	31	7:12	106.81	18.60	FLB, FRB, RLB, RRB	421356422, 421356451
270	316.19	31	16:40	253.43	20.31	FLB, FRB	421480269
283	323.77	31	16:56	256.16	16.47	FLB, FRB	422635427
291	328.36	31	17:08	257.82	13.45	FLB, FRB	423346401
322	345.50	31	17:25	264.52	8.92	FRB, FLB, RLB, RRB	426099261, 426099296
383	16.67	32	16:48	278.81	17.12	FRB, FLB, RLB, RRB	431511077, 431511104
439	43.10	32	16:44	289.18	16.55	NLB	ncam00548
474	59.00	32	16:52	293.41	13.90	NLB	ncam00548
582	107.94	32	16:41	296.45	15.83	NLB	ncam00548
610	121.23	32	17:34	291.85	4.25	NLB	ncam00550
751	197.46	32	16:28	264.00	23.24	FRB, FLB	464174522
765	206.07	32	16:49	260.16	18.24	FLB, FRB	465418782
782	216.73	32	16:59	255.97	15.72	FLB, FRB, RLB, RRB	466928832, 466928866
785	218.61	32	16:10	255.03	27.69	NLB	ncam00548
788	220.55	32	17:10	254.56	13.10	NLB	ncam00548
792	223.09	32	16:31	253.61	22.58	FLB, FRB, RLB, RRB	467815011, 467815060
806	232.09	32	16:27	250.61	23.32	NLB	ncam00548
813	236.64	32	17:09	249.67	13.49	FLB, FRB	469682237
814	237.29	32	16:55	249.46	16.70	FLB, FRB	469770196
815	237.93	32	16:46	249.23	18.71	FLB, FRB	469858472
819	240.53	32	16:45	248.58	18.91	FLB, FRB	470213649
824	243.77	32	16:02	246.89	28.79	FLB, FRB	470655026
828	246.40	32	16:46	247.31	18.68	FLB, FRB	471012999
830	247.49	32	16:28	246.77	22.74	FLB, FRB	471189532
924	307.50	32	16:21	250.39	24.74	NLB	ncam00548
1105	41.93	33	17:11	287.74	10.24	FLB, FRB	495606448
1114	46.05	33	16:41	290.29	17.15	FLB, FRB	496403367
1124	50.60	33	16:44	291.54	16.13	FLB, FRB	497291116
1130	53.33	33	17:18	290.95	8.08	FLB, FRB	497825752
1132	54.24	33	17:10	291.47	9.92	FLB, FRB	498002768
1137	56.49	33	16:45	293.10	15.56	FLB, FRB	498445016
1150	62.35	33	17:14	293.29	8.78	FLB, FRB	499600628
1157	65.49	33	17:13	293.95	8.88	FLB, FRB	500221886
1226	96.60	33	16:59	296.75	11.70	FLB, FRB	506345674
1258	111.42	33	16:39	296.01	16.44	NLB	ncam00548
1259	111.90	33	17:02	294.87	11.36	FLB, FRB	509275141
1261	112.82	33	16:01	298.19	25.02	NLB	ncam00548
1263	113.77	33	16:18	296.84	21.38	NLB	ncam00548
1268	116.15	33	16:36	295.27	17.30	NLB	ncam00548
1275	119.51	33	17:12	292.95	9.33	FLB, FRB	510696014
1287	125.30	33	16:30	293.42	19.22	FLB, FRB	511758612
1330	146.96	33	17:16	284.46	9.51	FLB, FRB	515578339
1332	147.99	33	16:40	285.36	18.14	FLB, FRB	515753675
1339	151.68	33	17:09	282.87	11.25	FLB, FRB	516376834
1358	161.91	33	17:35	278.09	5.34	FLB, FRB	518064970
1359	162.44	33	17:03	278.73	13.41	FLB, FRB	518151723
1378	173.02	33	16:46	274.64	18.00	FLB, FRB	519837215
1403	187.49	33	16:15	268.73	26.17	RLB, RRB	522054677
1405	188.69	33	16:38	267.79	20.48	FLB, FRB	522233564
1409	191.09	33	17:24	265.98	9.14	FLB, FRB, RLB, RRB	522591532, 522591583
1416	195.28	33	16:38	264.86	20.72	FLB, FRB	523210121
1418	196.50	33	17:16	263.83	11.31	FLB, FRB	523390041
1422	198.93	33	17:05	262.97	14.10	FLB, FRB, RLB, RRB	523744454, 523744503
1444	212.57	33	17:18	257.39	11.12	FLB, FRB, RLB, RRB	525698534, 525698583
1448	215.07	33	16:53	256.60	17.22	FLB, FRB	526052099
1454	218.88	33	17:04	255.18	14.60	FLB, FRB, RLB, RRB	526585575, 526585624
1474	231.71	33	17:21	250.98	10.57	FLB, FRB	528361546
1480	235.57	33	16:37	249.75	20.95	FLB, FRB	528892687
1484	238.19	33	17:30	249.22	8.64	FLB, FRB, RLB, RRB	529251205, 529251256
1491	242.74	33	17:17	248.23	11.55	FLB, FRB, RLB, RRB	529872102, 529872144
1493	244.04	33	17:11	247.95	13.03	FLB, FRB, RLB, RRB	530049331, 530049373
1496	246.01	33	17:35	247.48	7.38	FLB, FRB, RLB, RRB	530317281, 530317325
1504	251.23	33	17:28	246.64	8.97	FLB, FRB, RLB, RRB	531027377, 531027427
1511	255.78	33	16:42	245.76	19.61	FLB, FRB, RLB, RRB	531646212, 531646260
1512	256.42	33	16:28	245.42	22.63	FLB, FRB	531734165
1518	260.35	33	17:02	245.53	15.07	FLB, FRB	532269165
1537	272.68	33	17:17	245.24	11.64	FLB, FRB, RLB, RRB	533957634, 533957668
1555	284.18	33	16:47	245.83	18.45	NLB	ncam00548

Sol	Ls[°]	MY	LTST	Sun Azim. [°]	Sun Elev. [°]	Camera	SCLK/Sequence
1581	300.45	33	17:14	248.95	12.33	FLB, FRB, RLB, RRB	537865092, 537865126
1661	346.68	33	16:44	265.56	19.20	FLB, FRB	544965612
1668	350.22	33	17:15	266.69	11.29	FLB, FRB, RLB, RRB	545588880, 545588924
1675	353.89	33	16:57	268.62	15.86	FLB, FRB, RLB, RRB	546209039, 546209081
1681	357.01	33	16:46	270.20	18.40	FLB, FRB, RLB, RRB	546740938, 546740972
1715	14.15	34	16:34	278.18	20.70	FLB, FRB	549757840
1723	18.07	34	17:10	278.74	11.63	FLB, FRB, RLB, RRB	550470076, 550470111
1749	30.49	34	16:48	284.46	16.36	FLB, FRB, RLB, RRB	552776265, 552776300
1763	37.03	34	16:16	288.45	23.67	FLB, FRB	554016798
1764	37.50	34	16:46	287.15	16.40	FLB, FRB, RLB, RRB	554107432, 554107474
1765	37.97	34	17:16	286.21	9.12	FLB, FRB, RLB, RRB	554198056, 554198100
1770	40.27	34	16:18	289.50	22.85	FLB, FRB	554638225
1771	40.74	34	16:48	288.20	15.68	FLB, FRB, RLB, RRB	554728843, 554728878
1772	41.21	34	17:19	287.25	8.44	FLB, FRB, RLB, RRB	554819466, 554819510
1777	43.49	34	16:20	290.49	22.06	FLB, FRB	555259647
1779	44.42	34	17:21	288.22	7.71	FLB, FRB, RLB, RRB	555440886, 555440930
1791	49.88	34	16:31	291.98	19.26	FLB, FRB	556502839
1802	54.86	34	16:06	294.89	24.52	FLB, FRB	557477610
1805	56.23	34	16:38	293.36	17.14	FLB, FRB	557745889
1816	61.19	34	17:16	292.96	8.31	FLB, FRB, RLB, RRB	558724543, 558724579
1818	62.08	34	16:49	294.23	14.39	FLB, FRB	558901332
1821	63.42	34	16:28	295.59	19.01	FLB, FRB, RLB, RRB	559165415, 559165450
1824	64.78	34	16:55	294.52	12.89	FLB, FRB, RLB, RRB	559433352, 559433387
1831	67.92	34	17:07	294.62	10.12	FLB, FRB, RLB, RRB	560055379, 560055414
1836	70.17	34	17:18	294.58	7.53	FLB, FRB, RLB, RRB	560499871, 560499907
1838	71.06	34	17:01	295.39	11.49	FLB, FRB, RLB, RRB	560676312, 560676347
1839	71.49	34	16:09	298.29	22.90	FLB, FRB, RLB, RRB	560761909, 560761943
1845	74.19	34	16:41	296.73	15.71	FLB, FRB, RLB, RRB	561296467, 561296488
1848	75.53	34	16:19	298.17	20.55	FLB, FRB, RLB, RRB	561561352, 561561451
1849	75.81	34	07:27	62.56	17.74	NRB	ncam00581
1853	77.79	34	16:54	296.51	12.74	FLB, FRB, RLB, RRB	562007347, 562007382
1859	80.47	34	16:19	298.67	20.44	FLB, FRB, RLB, RRB	562537763, 562537797
1863	82.28	34	16:48	297.18	14.11	FLB, FRB, RLB, RRB	562894592, 562894627
1865	83.18	34	16:42	297.55	15.46	FLB, FRB, RLB, RRB	563071738, 563071766
1872	86.34	34	17:01	296.80	11.25	NRB	ncam00581
1879	89.51	34	17:02	296.76	10.81	FLB, FRB, RLB, RRB	564315716, 564315760
1885	92.21	34	16:05	299.99	23.33	FLB, FRB	564844795
1886	92.68	34	16:59	296.89	11.61	FLB, FRB, RLB, RRB	564936854, 564936898
1892	95.41	34	16:37	297.87	16.48	FLB, FRB, RLB, RRB	565468106, 565468141
1894	96.14	34	07:12	62.66	14.36	NRB	ncam00581
1895	96.78	34	16:37	297.78	16.40	FLB, FRB, RLB, RRB	565734434, 565734468
1902	100.00	34	17:12	295.98	8.73	FLB, FRB	566357944
1904	100.92	34	17:04	296.23	10.62	FLB, FRB, RLB, RRB	566534944, 566534987
1911	104.16	34	17:16	295.43	7.90	FLB, FRB, RLB, RBB	567157071, 567157100
1916	106.47	34	16:27	297.47	19.00	NRB	ncam00582
1924	110.02	34	06:59	64.76	11.59	NRB	ncam00581
1925	110.69	34	17:06	294.91	10.39	FLB, FRB, RLB, RRB	568399163, 568399191
1927	111.62	34	16:53	295.26	13.18	FLB, FRB	568575951
1928	112.08	34	16:20	297.01	20.77	FLB, FRB, RLB, RRB	568662583, 568662679
1929	112.58	34	17:31	293.73	4.75	RLB, RRB	568755797
1932	113.98	34	16:50	294.99	14.01	FLB, FRB, RLB, RRB	569019566, 569019601
1934	114.94	34	17:23	293.52	6.51	RLB, RRB	569199181
1935	115.41	34	16:53	294.59	13.45	FLB, FRB, RLB, RRB	569286026, 569286061
1937	116.36	34	16:53	294.40	13.51	FLB, FRB, RLB, RRB	569463546, 569463588
1938	116.83	34	16:57	294.11	12.56	RLB, RRB	569552596
1947	121.15	34	17:04	292.86	11.12	FLB, FRB, RLB, RRB	570351901, 570351944
1963	128.95	34	17:27	290.05	6.18	FLB, FRB, RLB, RRB	571773544, 571773587
1964	129.44	34	17:18	290.18	8.25	FLB, FRB, RLB, RRB	571861758, 571861809
1968	131.40	34	16:23	292.00	21.03	NRB	ncam00581
1969	131.91	34	17:05	289.92	11.42	FLB, FRB	572304802
1971	132.70	34	07:12	69.62	15.48	NRB	ncam00583
1971	132.91	34	17:14	289.28	9.28	FLB, FRB, RLB, RRB	572482889, 572482940
1972	133.40	34	16:45	290.26	16.04	FLB, FRB, RLB, RRB	572569883, 572569932
1973	133.91	34	17:03	289.36	11.86	FLB, FRB, RLB, RRB	572659745, 572659794
1974	134.41	34	17:12	288.90	9.90	FLB, FRB, RLB, RRB	572749030, 572749080
1975	134.90	34	16:39	290.06	17.55	FLB, FRB, RLB, RRB	572835795, 572835844
1978	136.41	34	16:49	289.11	15.28	FLB, FRB	573102731
1979	136.93	34	17:25	287.67	6.87	FLB, FRB, RLB, RRB	573193678, 573193723
1984	139.46	34	17:10	287.29	10.45	FLB, FRB, RLB, RRB	573636601, 573636651
1988	141.50	34	17:29	286.03	6.15	FLB, FRB, RLB, RRB	573992786, 573992829
1989	142.00	34	16:30	288.08	20.29	FLB, FRB, RLB, RRB	574077879, 574077965
1998	146.66	34	17:03	284.98	12.47	NRB	ncam00581
2000	147.69	34	16:49	285.12	16.02	FLB, FRB, RLB, RRB	575055503, 575055544
2001	148.22	34	17:05	284.32	12.04	FLB, FRB, RLB, RRB	575145295, 575145330

Table A2. Results of the retrieval

Sol	Lsl ^o I	MY	LTST	Sun Elev [°]	Cam	DHG, g ₁	DHG, g ₂	DHG, α	CYL, D/L	TAB, Dust Analog.	X ² _{red} DHG	X ² _{red} CYL	X ² _{red} TAB
269	315.37	31	7:12	18.60	HAZ	0.98 ^{+0.00} _{-0.00}	0.26 ^{+0.00} _{-0.00}	0.74 ^{+0.01} _{-0.01}	1.8	Palagonite	0.022	0.116	2.249
270	316.19	31	16:40	20.31	HAZ	0.94 ^{+0.03} _{-0.02}	0.33 ^{+0.05} _{-0.04}	0.61 ^{+0.05} _{-0.08}	1.5	Palagonite	0.048	0.010	2.199
283	323.77	31	16:56	16.47	HAZ	0.92 ^{+0.02} _{-0.01}	0.36 ^{+0.01} _{-0.00}	0.62 ^{+0.00} _{-0.01}	0.7	Basalt	0.013	0.011	2.784
291	328.36	31	17:08	13.45	HAZ	0.93 ^{+0.01} _{-0.00}	0.36 ^{+0.00} _{-0.00}	0.64 ^{+0.00} _{-0.03}	1.7	Basalt	0.017	0.044	4.000
322	345.50	31	17:25	8.92	HAZ	0.91 ^{+0.00} _{-0.00}	0.17 ^{+0.00} _{-0.00}	0.70 ^{+0.00} _{-0.00}	0.8	Basalt	0.099	0.024	4.450
383	16.67	32	16:48	17.12	HAZ	0.82 ^{+0.02} _{-0.02}	0.25 ^{+0.04} _{-0.04}	0.68 ^{+0.03} _{-0.05}	1.1	Basalt	0.043	0.144	1.212
439	43.10	32	16:44	16.55	NAV	0.92 ^{+0.00} _{-0.01}	0.17 ^{+0.00} _{-0.04}	0.74 ^{+0.02} _{-0.00}	2.3	Basalt	0.049	0.093	1.163
474	59.00	32	16:52	13.90	NAV	0.85 ^{+0.01} _{-0.02}	0.05 ^{+0.00} _{-0.04}	0.78 ^{+0.02} _{-0.00}	0.7	Basalt	0.042	0.025	0.948
582	107.94	32	16:41	15.83	NAV	0.88 ^{+0.01} _{-0.00}	0.02 ^{+0.04} _{-0.00}	0.82 ^{+0.00} _{-0.01}	1.0	Basalt	0.042	0.077	0.420
610	121.23	32	17:34	4.25	NAV	0.88 ^{+0.00} _{-0.01}	0.20 ^{+0.04} _{-0.04}	0.84 ^{+0.01} _{-0.02}	0.6	Palagonite	0.039	0.296	0.365
751	197.46	32	16:28	23.24	HAZ	0.89 ^{+0.09} _{-0.05}	0.09 ^{+0.09} _{-0.11}	0.71 ^{+0.07} _{-0.10}	1.9	Basalt	0.002	0.026	1.491
765	206.07	32	16:49	18.24	HAZ	0.99 ^{+0.00} _{-0.09}	0.26 ^{+0.00} _{-0.02}	0.51 ^{+0.04} _{-0.01}	1.6	Basalt	0.031	0.025	2.721
782	216.73	32	16:59	15.72	HAZ	0.90 ^{+0.09} _{-0.09}	0.09 ^{+0.08} _{-0.07}	0.63 ^{+0.16} _{-0.13}	1.8	Basalt	0.002	0.010	4.529
785	218.61	32	16:10	27.69	NAV	0.97 ^{+0.00} _{-0.00}	0.26 ^{+0.04} _{-0.00}	0.71 ^{+0.01} _{-0.01}	2.2	Basalt	0.036	0.286	0.601
788	220.55	32	17:10	13.10	NAV	0.77 ^{+0.03} _{-0.01}	-0.08 ^{+0.19} _{-0.15}	0.86 ^{+0.03} _{-0.07}	2.2	Basalt	0.035	0.113	3.417
792	223.09	32	16:31	22.58	HAZ	0.91 ^{+0.02} _{-0.03}	0.32 ^{+0.04} _{-0.04}	0.55 ^{+0.05} _{-0.05}	1.7	Basalt	0.051	0.011	2.867
806	232.09	32	16:27	23.32	NAV	0.98 ^{+0.00} _{-0.00}	0.26 ^{+0.00} _{-0.00}	0.71 ^{+0.01} _{-0.00}	2.2	Basalt	0.069	0.364	1.208
813	236.64	32	17:09	13.49	HAZ	0.91 ^{+0.08} _{-0.01}	0.02 ^{+0.16} _{-0.08}	0.79 ^{+0.11} _{-0.29}	0.6	Palagonite	0.008	0.008	2.025
814	237.29	32	16:55	16.70	HAZ	0.99 ^{+0.00} _{-0.07}	0.06 ^{+0.12} _{-0.00}	0.81 ^{+0.00} _{-0.31}	0.6	Palagonite	0.005	0.014	3.793
815	237.93	32	16:46	18.71	HAZ	0.98 ^{+0.01} _{-0.01}	0.10 ^{+0.04} _{-0.04}	0.69 ^{+0.06} _{-0.03}	0.6	Palagonite	0.001	0.005	4.958
819	240.53	32	16:45	18.91	HAZ	0.94 ^{+0.01} _{-0.01}	0.33 ^{+0.00} _{-0.00}	0.63 ^{+0.01} _{-0.00}	1.5	Palagonite	0.090	0.015	3.112
824	243.77	32	16:02	28.79	HAZ	0.92 ^{+0.02} _{-0.00}	0.36 ^{+0.05} _{-0.00}	0.53 ^{+0.01} _{-0.02}	1.7	Basalt	0.020	0.169	1.369
828	246.40	32	16:46	18.68	HAZ	0.94 ^{+0.01} _{-0.01}	0.33 ^{+0.00} _{-0.04}	0.61 ^{+0.03} _{-0.00}	1.4	Basalt	0.073	0.018	3.225
830	247.49	32	16:28	22.74	HAZ	0.82 ^{+0.02} _{-0.04}	0.25 ^{+0.09} _{-0.08}	0.96 ^{+0.00} _{-0.00}	1.4	Basalt	0.005	0.055	2.075
924	307.50	32	16:21	24.74	NAV	0.96 ^{+0.00} _{-0.00}	0.29 ^{+0.00} _{-0.00}	0.71 ^{+0.00} _{-0.00}	0.5	Basalt	0.101	0.178	0.113
1105	41.93	33	17:11	10.24	HAZ	0.96 ^{+0.00} _{-0.00}	0.25 ^{+0.00} _{-0.00}	0.67 ^{+0.01} _{-0.02}	1.7	Palagonite	0.123	0.008	2.278
1114	46.05	33	16:41	17.15	HAZ	0.81 ^{+0.18} _{-0.23}	-0.12 ^{+0.14} _{-0.23}	0.78 ^{+0.06} _{-0.03}	2.4	Basalt	0.003	0.012	2.844
1124	50.60	33	16:44	16.13	HAZ	0.77 ^{+0.15} _{-0.14}	-0.20 ^{+0.25} _{-0.27}	0.83 ^{+0.06} _{-0.05}	1.5	Basalt	0.003	0.021	2.395
1130	53.33	33	17:18	8.08	HAZ	0.97 ^{+0.02} _{-0.00}	0.30 ^{+0.05} _{-0.00}	0.71 ^{+0.05} _{-0.14}	1.7	Palagonite	0.021	0.168	1.879
1132	54.24	33	17:10	9.92	HAZ	0.94 ^{+0.01} _{-0.00}	0.21 ^{+0.00} _{-0.04}	0.66 ^{+0.06} _{-0.08}	1.5	Palagonite	0.097	0.005	2.773
1137	56.49	33	16:45	15.56	HAZ	0.73 ^{+0.03} _{-0.03}	-0.22 ^{+0.18} _{-0.16}	0.86 ^{+0.02} _{-0.05}	0.8	Basalt	0.005	0.007	1.289
1150	62.35	33	17:14	8.78	HAZ	0.97 ^{+0.01} _{-0.00}	0.38 ^{+0.00} _{-0.00}	0.64 ^{+0.02} _{-0.03}	1.8	Palagonite	0.068	0.073	1.743
1157	65.49	33	17:13	8.88	HAZ	0.96 ^{+0.00} _{-0.01}	0.33 ^{+0.00} _{-0.00}	0.69 ^{+0.01} _{-0.01}	1.7	Palagonite	0.144	0.074	2.272
1226	96.60	33	16:59	11.70	HAZ	0.91 ^{+0.01} _{-0.01}	0.50 ^{+0.01} _{-0.04}	0.57 ^{+0.05} _{-0.11}	1.7	Basalt	0.147	0.129	2.273
1258	111.42	33	16:39	16.44	NAV	0.91 ^{+0.01} _{-0.00}	0.24 ^{+0.04} _{-0.00}	0.71 ^{+0.00} _{-0.03}	2.0	Basalt	0.207	0.183	0.271
1259	111.90	33	17:02	11.36	HAZ	0.91 ^{+0.02} _{-0.03}	0.28 ^{+0.04} _{-0.01}	0.55 ^{+0.03} _{-0.05}	0.8	Basalt	0.117	0.014	2.067
1261	112.82	33	16:01	25.02	NAV	0.90 ^{+0.00} _{-0.00}	0.31 ^{+0.00} _{-0.04}	0.65 ^{+0.02} _{-0.01}	0.8	Basalt	0.189	0.108	0.166
1263	113.77	33	16:18	21.38	NAV	0.91 ^{+0.00} _{-0.00}	0.28 ^{+0.00} _{-0.00}	0.64 ^{+0.02} _{-0.01}	0.8	Basalt	0.194	0.102	0.239
1268	116.15	33	16:36	17.30	NAV	0.91 ^{+0.00} _{-0.00}	0.28 ^{+0.00} _{-0.04}	0.65 ^{+0.02} _{-0.01}	1.0	Basalt	0.191	0.073	0.258
1275	119.51	33	17:12	9.33	HAZ	0.79 ^{+0.03} _{-0.04}	0.02 ^{+0.07} _{-0.09}	0.82 ^{+0.03} _{-0.02}	0.8	Basalt	0.055	0.013	1.154
1287	125.30	33	16:30	19.22	HAZ	0.86 ^{+0.02} _{-0.02}	0.19 ^{+0.08} _{-0.09}	0.74 ^{+0.02} _{-0.04}	0.7	Basalt	0.015	0.017	0.198
1330	146.96	33	17:16	9.51	HAZ	0.87 ^{+0.06} _{-0.07}	0.05 ^{+0.03} _{-0.04}	0.71 ^{+0.09} _{-0.16}	1.8	Basalt	0.013	0.026	3.062
1332	147.99	33	16:40	18.14	HAZ	0.77 ^{+0.12} _{-0.06}	-0.08 ^{+0.13} _{-0.11}	0.78 ^{+0.05} _{-0.10}	1.7	Basalt	0.008	0.016	2.161
1339	151.68	33	17:09	11.25	HAZ	0.95 ^{+0.01} _{-0.01}	0.06 ^{+0.08} _{-0.00}	0.78 ^{+0.02} _{-0.22}	1.8	Palagonite	0.021	0.027	3.663
1358	161.91	33	17:35	5.34	HAZ	0.96 ^{+0.00} _{-0.01}	0.29 ^{+0.00} _{-0.04}	0.68 ^{+0.06} _{-0.01}	1.7	Palagonite	0.014	0.592	1.154
1359	162.44	33	17:03	13.41	HAZ	0.99 ^{+0.00} _{-0.00}	0.18 ^{+0.00} _{-0.00}	0.58 ^{+0.03} _{-0.03}	1.6	Basalt	0.038	0.026	3.886
1378	173.02	33	16:46	18.00	HAZ	0.83 ^{+0.04} _{-0.04}	-0.02 ^{+0.07} _{-0.07}	0.76 ^{+0.03} _{-0.04}	2.4	Basalt	0.010	0.031	1.861
1403	187.49	33	16:15	26.17	HAZ	0.98 ^{+0.01} _{-0.01}	0.26 ^{+0.00} _{-0.00}	0.69 ^{+0.10} _{-0.01}	2.3	Basalt	0.010	0.042	0.038
1405	188.69	33	16:38	20.48	HAZ	0.94 ^{+0.00} _{-0.00}	0.36 ^{+0.00} _{-0.00}	0.63 ^{+0.00} _{-0.01}	1.2	Basalt	0.015	0.087	0.267
1409	191.09	33	17:24	9.14	HAZ	0.96 ^{+0.00} _{-0.00}	0.41 ^{+0.00} _{-0.00}	0.67 ^{+0.00} _{-0.01}	1.7	Palagonite	0.098	0.678	2.079
1416	195.28	33	16:38	20.72	HAZ	0.77 ^{+0.04} _{-0.05}	-0.02 ^{+0.07} _{-0.05}	0.76 ^{+0.06} _{-0.05}	1.6	Basalt	0.005	0.006	2.224
1418	196.50	33	17:16	11.31	HAZ	0.95 ^{+0.01} _{-0.00}	0.41 ^{+0.00} _{-0.04}	0.59 ^{+0.00} _{-0.00}	1.7	Basalt	0.052	0.041	3.629
1422	198.93	33	17:05	14.10	HAZ	0.94 ^{+0.01} _{-0.01}	0.10 ^{+0.04} _{-0.00}	0.86 ^{+0.00} _{-0.01}	2.3	Basalt	0.014	0.121	1.017
1444	212.57	33	17:18	11.12	HAZ	0.94 ^{+0.02} _{-0.00}	0.06 ^{+0.04} _{-0.00}	0.84 ^{+0.03} _{-0.02}	1.8	Palagonite	0.007	0.005	1.672
1448	215.07	33	16:53	17.22	HAZ	0.97 ^{+0.02} _{-0.02}	0.26 ^{+0.00} _{-0.04}	0.55 ^{+0.07} _{-0.04}	1.7	Palagonite	0.019	0.024	3.090
1454	218.88	33	17:04	14.60	HAZ	0.94 ^{+0.00} _{-0.00}	0.33 ^{+0.00} _{-0.00}	0.59 ^{+0.00} _{-0.00}	1.2	Basalt	0.077	0.137	2.266
1474	231.71	33	17:21	10.57	HAZ	0.89 ^{+0.10} _{-0.01}	0.09 ^{+0.17} _{-0.04}	0.74 ^{+0.03} _{-0.24}	0.8	Palagonite	0.007	0.019	0.803
1480	235.57	33	16:37	20.95	HAZ	0.89 ^{+0.04} _{-0.01}	0.38 ^{+0.04} _{-0.0}						

Sol	Lst ^l	MY	LTST	Sun Elev ^l]	Cam	DHG, g ₁	DHG, g ₂	DHG, α	CYL, D/L	TAB, Dust Analog.	X ² _{red} DHG	X ² _{red} CYL	X ² _{red} TAB
1763	37.03	34	16:16	23.67	HAZ	0.97 ^{+0.01} _{-0.02}	0.14 ^{+0.00} _{-0.04}	0.70 ^{+0.03} _{-0.01}	2.2	Basalt	0.012	0.217	0.577
1764	37.50	34	16:46	16.40	HAZ	0.97 ^{+0.00} _{-0.01}	0.18 ^{+0.00} _{-0.00}	0.73 ^{+0.00} _{-0.00}	2.2	Basalt	0.140	0.059	1.046
1765	37.97	34	17:16	9.12	HAZ	0.81 ^{+0.00} _{-0.01}	-0.08 ^{+0.00} _{-0.06}	0.82 ^{+0.02} _{-0.00}	2.2	Basalt	0.122	0.097	2.709
1770	40.27	34	16:18	22.85	HAZ	0.98 ^{+0.00} _{-0.02}	0.14 ^{+0.00} _{-0.04}	0.73 ^{+0.03} _{-0.01}	2.2	Basalt	0.017	0.220	0.500
1771	40.74	34	16:48	15.68	HAZ	0.97 ^{+0.00} _{-0.01}	0.18 ^{+0.00} _{-0.00}	0.78 ^{+0.00} _{-0.00}	0.5	Basalt	0.107	0.335	0.706
1772	41.21	34	17:19	8.44	HAZ	0.84 ^{+0.00} _{-0.01}	-0.09 ^{+0.00} _{-0.10}	0.84 ^{+0.02} _{-0.00}	0.8	Basalt	0.086	0.008	3.742
1777	43.49	34	16:20	22.06	HAZ	0.95 ^{+0.03} _{-0.04}	0.10 ^{+0.04} _{-0.04}	0.75 ^{+0.02} _{-0.03}	2.2	Basalt	0.014	0.136	0.458
1779	44.42	34	17:21	7.71	HAZ	0.84 ^{+0.01} _{-0.01}	0.05 ^{+0.10} _{-0.03}	0.81 ^{+0.02} _{-0.04}	1.1	Basalt	0.097	0.032	3.325
1791	49.88	34	16:31	19.26	HAZ	0.93 ^{+0.05} _{-0.03}	0.09 ^{+0.09} _{-0.08}	0.79 ^{+0.04} _{-0.07}	2.2	Basalt	0.008	0.023	0.321
1802	54.86	34	16:06	24.52	HAZ	0.89 ^{+0.00} _{-0.01}	0.38 ^{+0.04} _{-0.00}	0.70 ^{+0.03} _{-0.00}	1.1	Basalt	0.031	0.174	0.525
1805	56.23	34	16:38	17.14	HAZ	0.97 ^{+0.00} _{-0.01}	0.49 ^{+0.00} _{-0.00}	0.66 ^{+0.11} _{-0.00}	1.9	Basalt	0.156	0.211	0.281
1816	61.19	34	17:16	8.31	HAZ	0.82 ^{+0.01} _{-0.01}	0.15 ^{+0.07} _{-0.03}	0.74 ^{+0.03} _{-0.04}	1.0	Palagonite	0.014	0.020	1.437
1818	62.08	34	16:49	14.39	HAZ	0.94 ^{+0.00} _{-0.01}	0.13 ^{+0.00} _{-0.04}	0.78 ^{+0.02} _{-0.01}	2.2	Basalt	0.025	0.110	0.771
1821	63.42	34	16:28	19.01	HAZ	0.96 ^{+0.00} _{-0.01}	0.33 ^{+0.00} _{-0.00}	0.60 ^{+0.00} _{-0.00}	1.2	Basalt	0.102	0.510	0.585
1824	64.78	34	16:55	12.89	HAZ	0.92 ^{+0.00} _{-0.01}	0.09 ^{+0.04} _{-0.04}	0.80 ^{+0.02} _{-0.00}	2.2	Basalt	0.035	0.054	0.889
1831	67.92	34	17:07	10.12	HAZ	0.76 ^{+0.01} _{-0.02}	-0.36 ^{+0.06} _{-0.08}	0.85 ^{+0.01} _{-0.01}	1.4	Basalt	0.012	0.031	2.634
1836	70.17	34	17:18	7.53	HAZ	0.86 ^{+0.01} _{-0.01}	0.09 ^{+0.04} _{-0.05}	0.77 ^{+0.00} _{-0.00}	1.8	Basalt	0.147	0.016	2.852
1838	71.06	34	17:01	11.49	HAZ	0.72 ^{+0.00} _{-0.00}	-0.31 ^{+0.03} _{-0.00}	0.86 ^{+0.00} _{-0.01}	0.5	Basalt	0.064	0.398	1.282
1839	71.49	34	16:09	22.90	HAZ	0.94 ^{+0.04} _{-0.01}	0.02 ^{+0.04} _{-0.00}	0.72 ^{+0.01} _{-0.04}	2.3	Basalt	0.011	0.012	0.822
1845	74.19	34	16:41	15.71	HAZ	0.76 ^{+0.00} _{-0.01}	-0.48 ^{+0.03} _{-0.12}	0.91 ^{+0.11} _{-0.00}	2.0	Basalt	0.087	0.160	0.970
1848	75.53	34	16:19	20.55	HAZ	0.95 ^{+0.00} _{-0.00}	0.14 ^{+0.00} _{-0.00}	0.74 ^{+0.00} _{-0.00}	2.0	Basalt	0.021	0.295	0.782
1849	75.81	34	07:27	17.74	NAV	0.86 ^{+0.00} _{-0.00}	-0.05 ^{+0.04} _{-0.04}	0.85 ^{+0.01} _{-0.01}	2.3	Basalt	0.050	0.110	0.231
1853	77.79	34	16:54	12.74	HAZ	0.70 ^{+0.01} _{-0.01}	-0.33 ^{+0.05} _{-0.06}	0.88 ^{+0.01} _{-0.01}	1.0	Basalt	0.077	0.231	1.010
1859	80.47	34	16:19	20.44	HAZ	0.97 ^{+0.00} _{-0.01}	0.14 ^{+0.00} _{-0.04}	0.69 ^{+0.01} _{-0.00}	2.0	Basalt	0.203	0.141	0.560
1863	82.28	34	16:48	14.11	HAZ	0.71 ^{+0.01} _{-0.01}	-0.33 ^{+0.05} _{-0.09}	0.89 ^{+0.01} _{-0.01}	2.0	Basalt	0.114	0.360	0.888
1865	83.18	34	16:42	15.46	HAZ	0.81 ^{+0.00} _{-0.01}	0.38 ^{+0.00} _{-0.00}	0.64 ^{+0.00} _{-0.00}	2.1	Basalt	0.257	0.060	0.493
1872	86.34	34	17:01	11.25	NAV	0.85 ^{+0.01} _{-0.01}	-0.23 ^{+0.07} _{-0.00}	0.91 ^{+0.00} _{-0.01}	2.3	Basalt	0.029	0.037	0.372
1879	89.51	34	17:02	10.81	HAZ	0.97 ^{+0.00} _{-0.01}	0.06 ^{+0.00} _{-0.00}	0.88 ^{+0.00} _{-0.00}	2.0	Basalt	0.027	0.101	0.732
1885	92.21	34	16:05	23.33	HAZ	0.92 ^{+0.00} _{-0.01}	0.13 ^{+0.00} _{-0.04}	0.70 ^{+0.02} _{-0.01}	2.3	Basalt	0.031	0.047	0.639
1886	92.68	34	16:59	11.61	HAZ	0.66 ^{+0.04} _{-0.03}	-0.15 ^{+0.19} _{-0.17}	0.88 ^{+0.04} _{-0.06}	2.2	Basalt	0.021	0.095	1.239
1892	95.41	34	16:37	16.48	HAZ	0.97 ^{+0.00} _{-0.01}	0.26 ^{+0.00} _{-0.01}	0.71 ^{+0.00} _{-0.03}	2.0	Basalt	0.069	0.349	0.497
1894	96.14	34	07:12	14.36	NAV	0.90 ^{+0.00} _{-0.00}	0.02 ^{+0.00} _{-0.04}	0.85 ^{+0.01} _{-0.00}	2.3	Basalt	0.065	0.023	0.166
1895	96.78	34	16:37	16.40	HAZ	0.78 ^{+0.01} _{-0.00}	-0.40 ^{+0.06} _{-0.00}	0.91 ^{+0.00} _{-0.01}	2.0	Basalt	0.101	0.038	0.874
1902	100.00	34	17:12	8.73	HAZ	0.89 ^{+0.08} _{-0.01}	0.24 ^{+0.08} _{-0.10}	0.66 ^{+0.20} _{-0.16}	0.8	Palagonite	0.006	0.017	0.876
1904	100.92	34	17:04	10.62	HAZ	0.85 ^{+0.00} _{-0.02}	0.16 ^{+0.00} _{-0.04}	0.62 ^{+0.00} _{-0.01}	2.3	Basalt	0.063	0.037	1.854
1911	104.16	34	17:16	7.90	HAZ	0.85 ^{+0.00} _{-0.00}	-0.05 ^{+0.03} _{-0.00}	0.82 ^{+0.00} _{-0.01}	0.7	Basalt	0.080	0.040	2.814
1916	106.47	34	16:27	19.00	NAV	0.85 ^{+0.01} _{-0.01}	0.02 ^{+0.07} _{-0.00}	0.83 ^{+0.03} _{-0.03}	1.0	Basalt	0.086	0.036	0.237
1924	110.02	34	06:59	11.59	NAV	0.90 ^{+0.01} _{-0.01}	0.09 ^{+0.04} _{-0.00}	0.82 ^{+0.00} _{-0.03}	2.3	Basalt	0.034	0.152	0.439
1925	110.69	34	17:06	10.39	HAZ	0.90 ^{+0.01} _{-0.03}	0.35 ^{+0.00} _{-0.00}	0.50 ^{+0.04} _{-0.00}	0.8	Basalt	0.296	0.038	1.505
1927	111.62	34	16:53	13.18	HAZ	0.91 ^{+0.06} _{-0.04}	-0.13 ^{+0.07} _{-0.07}	0.87 ^{+0.01} _{-0.02}	2.0	Basalt	0.011	0.066	1.157
1928	112.08	34	16:20	20.77	HAZ	0.95 ^{+0.03} _{-0.00}	0.06 ^{+0.04} _{-0.08}	0.76 ^{+0.07} _{-0.04}	2.2	Basalt	0.006	0.040	0.286
1929	112.58	34	17:31	4.75	HAZ	0.95 ^{+0.00} _{-0.00}	0.37 ^{+0.00} _{-0.00}	0.68 ^{+0.00} _{-0.01}	1.7	Palagonite	0.084	0.673	2.514
1932	113.98	34	16:50	14.01	HAZ	0.93 ^{+0.00} _{-0.01}	0.13 ^{+0.00} _{-0.00}	0.76 ^{+0.00} _{-0.00}	2.0	Basalt	0.202	0.114	0.637
1934	114.94	34	17:23	6.51	HAZ	0.90 ^{+0.00} _{-0.01}	0.17 ^{+0.04} _{-0.00}	0.76 ^{+0.00} _{-0.02}	1.8	Palagonite	0.083	0.057	1.790
1935	115.41	34	16:53	13.45	HAZ	0.66 ^{+0.01} _{-0.01}	-0.66 ^{+0.01} _{-0.01}	0.90 ^{+0.00} _{-0.01}	2.0	Basalt	0.135	0.071	0.722
1937	116.36	34	16:53	13.51	HAZ	0.94 ^{+0.00} _{-0.01}	0.17 ^{+0.00} _{-0.00}	0.77 ^{+0.01} _{-0.00}	2.0	Basalt	0.141	0.057	0.427
1938	116.83	34	16:57	12.56	HAZ	0.70 ^{+0.00} _{-0.01}	-0.70 ^{+0.03} _{-0.00}	0.86 ^{+0.00} _{-0.01}	2.0	Basalt	0.011	0.077	0.495
1947	121.15	34	17:04	11.12	HAZ	0.63 ^{+0.00} _{-0.00}	-0.63 ^{+0.00} _{-0.00}	0.95 ^{+0.00} _{-0.00}	2.1	Basalt	0.268	0.401	0.275
1963	128.95	34	17:27	6.18	HAZ	0.91 ^{+0.00} _{-0.00}	0.17 ^{+0.00} _{-0.00}	0.85 ^{+0.00} _{-0.00}	0.6	Palagonite	0.130	0.392	0.329
1964	129.44	34	17:18	8.25	HAZ	0.93 ^{+0.00} _{-0.01}	0.32 ^{+0.00} _{-0.00}	0.76 ^{+0.01} _{-0.01}	0.6	Palagonite	0.077	0.123	0.750
1968	131.40	34	16:23	21.03	NAV	0.78 ^{+0.01} _{-0.01}	-0.18 ^{+0.09} _{-0.06}	0.89 ^{+0.01} _{-0.02}	0.8	Basalt	0.011	0.013	0.251
1969	131.91	34	17:05	11.42	HAZ	0.72 ^{+0.00} _{-0.00}	-0.72 ^{+0.03} _{-0.00}	0.87 ^{+0.01} _{-0.00}	2.0	Basalt	0.100	0.161	0.246
1971	132.70	34	07:12	15.48	NAV	0.89 ^{+0.01} _{-0.00}	-0.05 ^{+0.04} _{-0.04}	0.88 ^{+0.01} _{-0.01}	1.9	Palagonite	0.147	0.081	1.123
1971	132.91	34	17:14	9.28	HAZ	0.76 ^{+0.01} _{-0.02}	-0.11 ^{+0.03} _{-0.15}	0.88 ^{+0.03} _{-0.01}	1.1	Basalt	0.038	0.043	0.197
1972	133.40	34	16:45	16.04	HAZ	0.95 ^{+0.00} _{-0.01}	0.25 ^{+0.00} _{-0.00}	0.76 ^{+0.00} _{-0.00}	1.9	Basalt	0.203	0.190	0.154
1973	133.91	34	17:03	11.86	HAZ	0.97 ^{+0.00} _{-0.01}	0.30 ^{+0.00} _{-0.00}	0.78 ^{+0.00} _{-0.00}	2.2	Basalt	0.231	0.178	0.266
1974	134.41	34	17:12	9.90	HAZ	0.74 ^{+0.01} _{-0.00}	-0.37 ^{+0.09} _{-0.03}	0.93 ^{+0.00} _{-0.01}	0.5	Basalt	0.007	0.067	0.982
1975	134.90	34	16:39	17.55	HAZ	0.96 ^{+0.00} _{-0.00}	0.33 ^{+0.00} _{-0.00}	0.70 ^{+0.00} _{-0.0}					